High-Resolution ENDOR Studies on Vanadyl Porphyrins and Crude-Oil Petroporphyrins

Donald Mannikko

A dissertation submitted in partial fulfillment of the requirements for the degree of

Doctor of Philosophy

University of Washington

2020

Reading Committee

Stefan Stoll, Chair

Joshua Vaughan

Bruce Robinson

Program Authorized to Offer Degree:

Chemistry

University of Washington

Abstract

High-Resolution ENDOR Studies on Vanadyl Porphyrins and Crude-Oil Petroporphyrins

Donald Mannikko

Chair of the Supervisory Committee:
Associate Professor Stefan Stoll
Chemistry

An open area of inquiry in chemistry research is the chemical environment surrounding vanadyl ions and particularly vanadyl porphyrins in crude oil. This is of interest due to the deleterious effect vanadyl has upon the catalytic efficiency of the chemical processes used to “upgrade” oil through contemporary refining practices. This dissertation describes the first steps towards developing a new method of non-destructive separation-free speciation of vanadyl porphyrins in crude oil through high-resolution electron nuclear double resonance (ENDOR) spectroscopy. The first two chapters describe the physical parameters of interest that are measured with Electron Paramagnetic Resonance (EPR), and a review of the research into vanadyl in crude oil. The development of the new method begins in Chapter 3 with the introduction of chemically relevant vanadyl porphyrins, and the complete analysis of their experimentally determined magnetic parameters. Chapter 4 describes the effort of combining the high-resolution ENDOR spectra with a series of mathematical models that allow analysis of these complicated mixtures of vanadyl porphyrins in crude oil.

TABLE OF CONTENTS

CHAPTER 1: EPR OBSERVABLES AND EXPERIMENTAL CONSIDERATIONS

Abstract

This introductory chapter discusses the theoretical basis for electron paramagnetic resonance (EPR) properties, and their interpretation. It discusses technical considerations for experimental choices in continuous-wave (CW) and pulse EPR. Additionally, it describes the pulse sequence and measured observables for pulse electron nuclear double resonance (ENDOR) experiments.

1.1 MAGNETIC INTERACTIONS

Electron Paramagnetic Resonance (EPR) is a powerful spectroscopic technique. EPR takes advantage of the intrinsic spin property of electrons. The spin of an electron can be analogized to a rotating point charge, which creates a magnetic field. When electrons are paired in a spatial molecular orbital, they necessarily have opposite directions of spin, and the individual magnetic fields cancel becoming diamagnetic. When an electron is unpaired in a spatial orbital it is paramagnetic. The vast majority of molecular electrons form these diamagnetic pairs to which EPR is fundamentally blind. This blindness is one of the primary strengths of EPR; the only entities visible by EPR in potentially complicated molecular systems are the unpaired electrons and their interactions with the local environment.

In the absence of a magnetic field, the orientations of the magnetic moments of unpaired electrons are stochastically disordered. When placed in a magnetic field, the magnetic moments of individual unpaired electrons tend toward aligning both parallel and antiparallel (following Boltzmann statistics) to the magnetic field. The electrons with their magnetic moment parallel to the magnetic field are lower in energy and therefore more populated. The magnetic moment of electrons points in the opposite direction of their spin; therefore, the lower-energy electrons with magnetic moment parallel and spin antiparallel to the applied magnetic field are often called β or spin down. The electrons with their magnetic moments antiparallel and spin parallel to the field are referred to as α or spin up. The population difference between spin-up and -down electrons is often called bulk magnetization, and conceptually is often the only model needed to conceptualize many EPR experiments.

As mentioned above, the difference in population between the spin-up and -down electrons follow Boltzmann statistics; therefore, the population difference depends on the temperature of the electron ensemble, and more importantly for this work, the magnitude and types of interactions between the electrons, the electrons' environment and the applied magnetic field.

For many molecular systems the strongest unpaired electron interaction is the so-called electron Zeeman effect. This is the interaction between the unpaired electron and an applied magnetic field. The magnitude of the interaction is directly proportional to the magnitude of the applied magnetic field. The spin Hamiltonian for the electron Zeeman interaction is

$$\mathcal{H}_{\mathrm{eZ}} = \mu_{\mathrm{B}} \boldsymbol{B}^{\mathrm{T}} g_{\mathrm{e}} \hat{\boldsymbol{S}} \tag{1}$$

where μ_{B} is the Bohr magneton, $\boldsymbol{B}$ is the column vector of the applied magnetic field, g_{e} is the electron g value, a physical constant known to incredibly high precision, and $\hat{\boldsymbol{S}}$ is the electron spin vector operator.

In practice, electrons are coupled to the local chemical environment, and that coupling is measurable by a change in the g_{e} term. In a chemical system g_{e} is replaced by $\boldsymbol{g}$, a 3x3 matrix that contains information about the electron's local environment. The matrix behaves mathematically as a tensor and therefore a coordinate transformation (frame rotation) can be applied such that the diagonal positions are the only non-zero components in the matrix. These three values are known as the principal components of the tensor.

$$\boldsymbol{g} = \begin{bmatrix} g_{xx} & g_{xy} & g_{xz} \\ g_{yx} & g_{yy} & g_{yz} \\ g_{zx} & g_{zy} & g_{zz} \end{bmatrix} \xrightarrow[\text{frame rotation}]{} \begin{bmatrix} g_{x} & 0 & 0 \\ 0 & g_{y} & 0 \\ 0 & 0 & g_{z} \end{bmatrix}$$

where g_{ij} are the components of the tensor in a general coordinate frame, and g_k are the components of the tensor in the principal-axis frame.

There are three potential symmetries of a tensor in the principal-axis frame. These situations are described for the g tensor but can be used for any interaction tensor in EPR. The first is when $g_x = g_y = g_z$. This is referred to as isotropic, which means that the measured value of g is independent of the molecular orientation. The second scenario is an axial tensor, when one principal value is unique (by convention the g_z term). Finally, when all three components are unique, the tensor is called rhombic. The three possible tensor symmetries are shown in Figure 1.

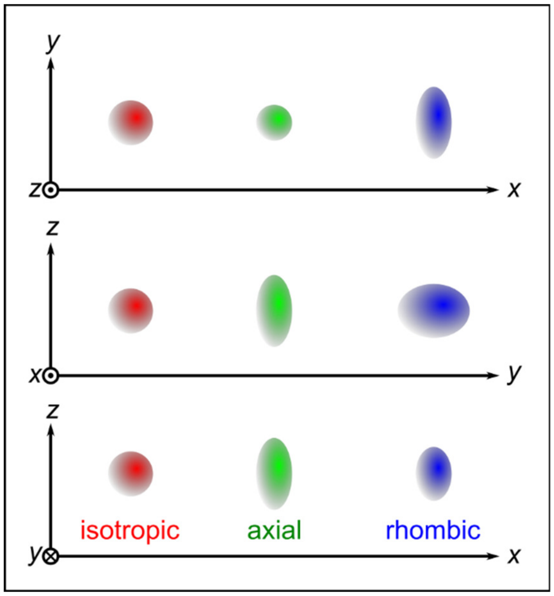

Figure 1. The three possible tensor symmetries depicted within the right-handed principal axes frame of the tensor. The red tensor is isotropic and therefore identical for each orientation. The green tensor is axial, and the unique axis is seen looking along the *z* axis on to the *xy*-plane. The blue tensor is rhombic, and therefore unique in all three axes.

The values of $\boldsymbol{g}$ are related to the angular momentum experienced by the unpaired electron due to spin–orbit coupling. In organic radicals the terms in $\boldsymbol{g}$ are shifted slightly away from g_e. Moving down the periodic table, unpaired electrons localized on heavier transition metals shift further away from g_e due to the increased spin–orbit coupling. The shift away from g_e is often orientation dependent and depending on experimental resolution can give insight into the singly occupied molecular orbital (SOMO) occupied by the unpaired electron.

Many nuclei also contain an intrinsic spin. Therefore, nuclei align in a magnetic field similar to the unpaired electrons. The magnetic moments of nuclei are much smaller than the magnetic moment of an unpaired electron so the nuclear Zeeman interaction is weaker than the analogous electron Zeeman interaction. The spin Hamiltonian for the nuclear Zeeman interaction is

$$\mathcal{H}_\mathrm{nZ} = -g_\mathrm{n}\mu_\mathrm{B}\boldsymbol{B}^\mathrm{T}\hat{\boldsymbol{I}} \tag{2}$$

where g_n is the nuclear g factor for the magnetic nucleus of interest, and $\hat{\boldsymbol{I}}$ is the nuclear spin vector operator. A chemical-shift tensor similar to the g tensor described above is present for the nuclei. However, the magnitude of the chemical shift is orders of magnitude smaller than the other anisotropies in the system (g tensor, hyperfine —see below); therefore, it is acceptable to neglect the effect of chemical shifts in the EPR spin Hamiltonian.

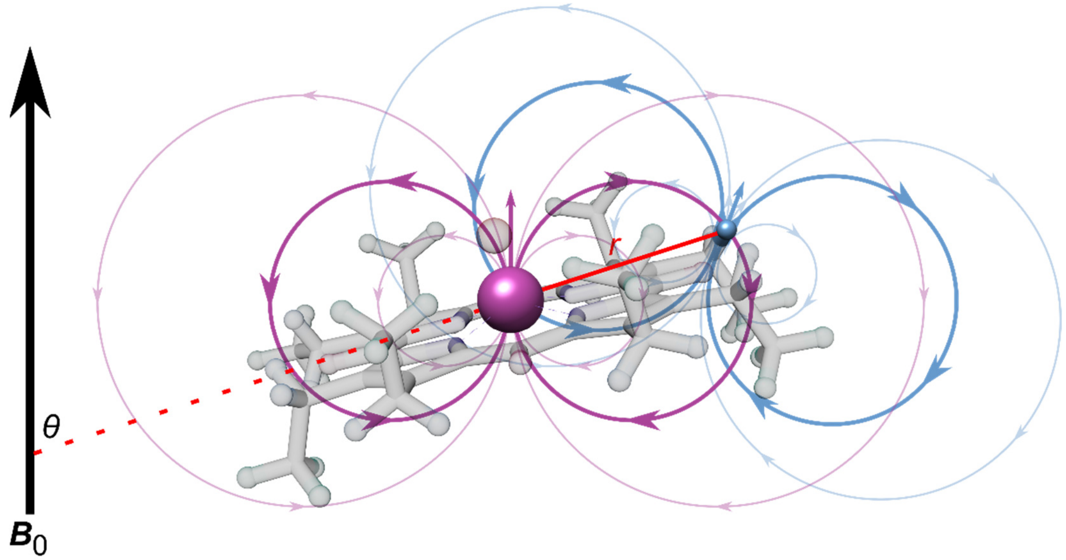

Figure 2. The dipolar interaction for a single orientation between the unpaired electron centered on the vanadyl ion (assuming the point-dipole approximation) and an individual proton on the porphyrin ligand. The distance between the electron and the proton (*r*) is shown in red. The angle (θ) between the vector connecting the electron to the nucleus and the externally applied magnetic field ($\boldsymbol{B}_0$) is shown in black.

The two Zeeman terms describe the interactions between the external magnetic field and the electron and nuclear spins. For chemists, often the most interesting interaction is the interaction between the unpaired electron and the surrounding magnetic nuclei. This interaction is referred to as hyperfine coupling. The spin Hamiltonian for the hyperfine coupling is

$$\mathcal{H}_{\mathrm{hc}} = h\hat{\boldsymbol{S}}^{\mathrm{T}}\boldsymbol{A}\hat{\boldsymbol{I}} \tag{3}$$

where h is the Planck constant; ***A*** is a 3x3 matrix that like the *g* matrix above behaves as a tensor. The components of ***A*** describe the interaction between the electron spin ***S*** and nuclear spin ***I*.**

The interaction describes a combination of through-space dipolar coupling and the so-called Fermi contact coupling, which in the principal-axis frame of the tensor can be written as

$$\boldsymbol{A}_{\mathrm{T}} = \begin{bmatrix} A_1 & 0 & 0 \\ 0 & A_2 & 0 \\ 0 & 0 & A_3 \end{bmatrix} = \begin{bmatrix} a_{\mathrm{c}} - T & 0 & 0 \\ 0 & a_{\mathrm{c}} - T & 0 \\ 0 & 0 & a_{\mathrm{c}} + 2T \end{bmatrix} = a_c\boldsymbol{I} + \boldsymbol{T}_{\mathrm{T}} \tag{4}$$

where a_{c} is the isotropic Fermi contact coupling constant, T is the anisotropic dipolar coupling constant, $\boldsymbol{I}$ is the 3x3 identity matrix, and $\boldsymbol{T}_{\mathrm{T}}$ is the dipolar coupling tensor in its principal-axis frame. The dipolar coupling is analogous to the classical through-space interaction of two magnetic dipoles as shown in Figure 2 and is described by the equation

$$\boldsymbol{T} = \frac{1}{4\pi h}\mu_0\mu_{\mathrm{n}}g_{\mathrm{n}}\mu_{\mathrm{e}}g_{\mathrm{e}}\left\langle\frac{3\boldsymbol{n}\cdot\boldsymbol{n}^{\mathrm{T}} - \boldsymbol{I}}{r^3}\right\rangle \tag{5}$$

where $\boldsymbol{n}$ is the unit vector of the vector pointing between the electron and the nucleus of interest; r is the distance between the electron and the nucleus of interest, and the brackets denote integration over the wavefunction to account for the delocalization of the electron. The tensor in Equation 5 is defined in an arbitrary frame, it reduced to $\boldsymbol{T} = \boldsymbol{T}_{\mathrm{T}}$ in the principal-axis frame.

The Fermi contact coupling is due to electron spin density at the location of the magnetic nucleus of interest. The Fermi contact coupling constant is described by

$$a_{\mathrm{c}} = \frac{2}{3h}\mu_0\mu_{\mathrm{n}}g_{\mathrm{n}}\mu_{\mathrm{B}}g_{\mathrm{e}}\,\rho^{\alpha-\beta}(\boldsymbol{R}) \tag{6}$$

where $\rho^{\alpha-\beta}(\boldsymbol{R})$ is the electron spin density (excess of α electron density over β electron density) on the nucleus of interest.

The separation of the principal values of ***A*** into through-space and contact contributions allows a deeper analysis of the hyperfine interaction. Estimates of electron spin density, electron–nuclear distance and even molecular orientation can be made through careful analysis of the hyperfine tensor.

These are the some of the most common magnetic interactions involved in EPR. The extraction of these interactions from an EPR spectrum and their analysis in terms of molecular and electronic structure is the primary goal of the EPR spectroscopist. Part of extracting these interactions requires an understanding of the type of experiment that generated the spectrum in the first place. The details of a given EPR experiment can quickly become quite complicated; however, fundamentally, all EPR experiments come down to applying two or more magnetic fields to a system with unpaired electrons and measuring the system's response.

The magnetic field that is ubiquitous through EPR is the *static magnetic field* ($\boldsymbol{B}_0$) that is generally used to generate the Zeeman splittings mentioned above. The second magnetic field is the *oscillating magnetic field* ($\boldsymbol{B}_1$) generated by (most often) microwave photons. When the energy gap of the up and down electrons approaches the photon energy of the microwave magnetic field, the unpaired electrons begin oscillating between the up and down states, this is referred to as the resonance condition. The energy that drives this resonance is absorbed from the microwave magnetic field. Additional magnetic fields can be added to probe other magnetic interactions as will be described below.

1.2 CONTINUOUS-WAVE EPR

The most common EPR experiment is continuous-wave (CW) EPR. As described above the CW experiment utilizes a static and a microwave magnetic field. Fundamentally the resonance condition can be generated by sweeping the static magnetic field with a constant microwave frequency of the microwave magnetic field, or sweeping the frequency of the microwave field while maintaining a stationary static field. Due to the limited bandwidth of microwave components the far more common experimental setup involves a constant-frequency microwave magnetic field and sweeping the static magnetic field.

The static magnetic field in CW EPR is swept over a range of individual magnetic field values. At each static field point the electron spins reach the Boltzmann equilibrium of up and down spins, the applied microwave magnetic field acts as a continuous low-power perturbation on the electron spin equilibrium. The amount of energy absorbed by the spin system is directly dependent on how many spins are experiencing the resonance condition for a given magnetic field value and microwave frequency.

More specifically, the signal intensity of an EPR spectrum is directly dependent upon the difference in population of the spin-up and -down electron states. The Boltzmann population ratio for spins in most contemporary EPR instrumentation is close to 1 (e.g. 0.95 for a g value of 2, field of 0.35 T, and temperature of 10 K); therefore, fundamentally the signal is small. To overcome the weak signal of EPR transitions, several clever engineering methods are utilized. Two of the most important to understand (because they effect the overall data collection and analysis) are the usage of resonators, and lock-in detection.

The majority of EPR experiments are performed with the experimental sample being centered in a resonator. Resonators are designed to build a standing electromagnetic wave focusing the oscillating magnetic field onto (and separating the electric field from) the sample. The effect of this separation focuses the magnetic field on the sample while simultaneously reducing interactions with electric dipoles in the sample.

Another way that signal intensity is maximized in EPR is by using lock-in detection. The static magnetic field is swept around each individual field position in sinusoidal fashion at a specific modulation frequency (often 100 kHz) and modulation amplitude. The signal reaching the detector is filtered and all frequencies except for the modulation frequency are removed. The signal remaining after demodulation contains information about the slope of the underlying absorbance signal within the modulation amplitude. Due to lock-in detection measuring the slope at each field position, the acquired signal is approximately the first derivative of the underlying absorption spectrum. As the magnitude of the modulation amplitude increases, the measured signal also increases; however, if the underlying spectral lineshape is narrower than the modulation amplitude, an artificial broadening will occur. The optimal choice for modulation amplitude for each CW experiment is an amplitude that simultaneously maximizes the signal while not introducing any additional broadening.

1.3 ENDOR

For technical reasons, the introduction of pulse EPR experiments has lagged significantly behind the analogous Nuclear Magnetic Resonance (NMR) instrumentation. This is primarily due to the difficulty in dealing with the orders of magnitude higher frequency requirements (GHz vs. MHz). However, pulse EPR contains a robust set of methods that can probe nearly every aspect of magnetic interactions.[1]

There are similarities between the fundamentals of CW and pulse EPR. These include the usage of static magnetic fields, the use of a resonator to maximize signal intensity, generating microwave magnetic fields with photon energy near the energy gap of the unpaired electrons in the static magnetic field, and more. The primary difference between the two approaches is that in pulse EPR the $\boldsymbol{B}_1$ field is applied with high power and short duration. The pulses are powerful enough that they can no longer be considered simple perturbations on the equilibrium of electron spins in a static magnetic field, and instead time-dependent quantum mechanics is required to simulate experimental observables.

The finite time length of excitation pulses adds an additional parameter of concern for pulse EPR experiments, namely pulse bandwidth. The pulse bandwidth is approximately the width of the Fourier transform of the excitation pulse, for example the most common pulse shape in pulse EPR is the rectangular pulse which yields a sinc function excitation bandwidth. A rough rule of thumb for excitation bandwidth is simply 1/pulse length, for example a 20 ns excitation pulse has ≈ 50 MHz excitation bandwidth. Most spin centers have unpaired electrons that resonate with a distribution of frequencies orders of magnitude larger than the possible excitation bandwidth of available pulses. Additionally, the use of resonators limits the possible excitation bandwidths to the bandwidth of the resonator itself.

The spectral bandwidth of short excitation pulses commonly used in EPR results in a rapid decay (relative to NMR timescales) of the free induction decay (FID) signal, often before detection is possible due to instrumentation dead time (on the order of 100 ns). To overcome this limitation, it is common practice to use echo detection. A given pulse sequence generates a signal that is a function of the overall bulk magnetization of the unpaired electrons, and because the signal is a refocusing of the free induction decay it is referred to as an echo.

The pulse technique of interest for this work is known as electron nuclear double resonance (ENDOR). As the name suggests, it is an EPR technique that uses magnetic excitation fields with two different frequencies. The first magnetic field is created by the microwave source with a frequency energetically similar to the energy gap of unpaired electrons ($\approx$ 9.5 GHz at 0.350 T). The frequency of the second magnetic field has a photon energy near the energy gap between the up and down states of magnetic nuclei ($\approx$ 15 MHz at 0.350 T for protons).

The original ENDOR experiments were performed with CW sources in 1956 by Feher.[2] Nearly a decade later in 1965 Mims introduced the first pulse ENDOR experiment and about a decade after that in 1974 Davies created another ENDOR pulse sequence that is widely used today.[3,4] The fundamental difference between the two pulse techniques involves the magnitude of hyperfine coupling they are capable of measuring. The sequence described by Mims is ideal for small hyperfine couplings $\lessapprox$ 3 MHz. The pulse sequence that Davies came up with is better for larger hyperfine values.

The Mims ENDOR pulse sequence is used for this work. The pulse sequence is shown in Figure 3. Three $\pi/2$ pulses in the microwave frequency generate a so-called stimulated echo. The observable of interest in the Mims ENDOR experiment is the integral of the stimulated echo. The echo appears at τ after the final pulse where τ is the spacing in time between the first two pulses. The initial $\pi/2$ pulse brings the equilibrium magnetization to the *xy* plane. During τ the magnetization spreads out in the *xy* plane due to the spread in electron resonance frequencies. The spread-out magnetization is moved back to the *z* axis by the second $\pi/2$ pulse. It's magnetization along *z* is stored over the time *T*, and the magnetization in the *xy* plane decays, and then the third $\pi/2$ pulse moves the magnetization back down to the *xy* plane once again. At a time τ after the final pulse the magnetization refocuses into the stimulated echo. During the delay *T*, a RF frequency pulse is applied. If the RF pulse resonates with a nucleus that is coupled to the unpaired electron, the local magnetic environment of the electron is altered (by flipping the coupled nucleus). The change in the electron's magnetic environment changes the resonant frequency of the electron; therefore, the electron will not refocus with the other electrons resulting in a decrease of echo intensity. The ENDOR experiment is performed by sweeping through a RF range of interest for a given magnitude of nuclear coupling.

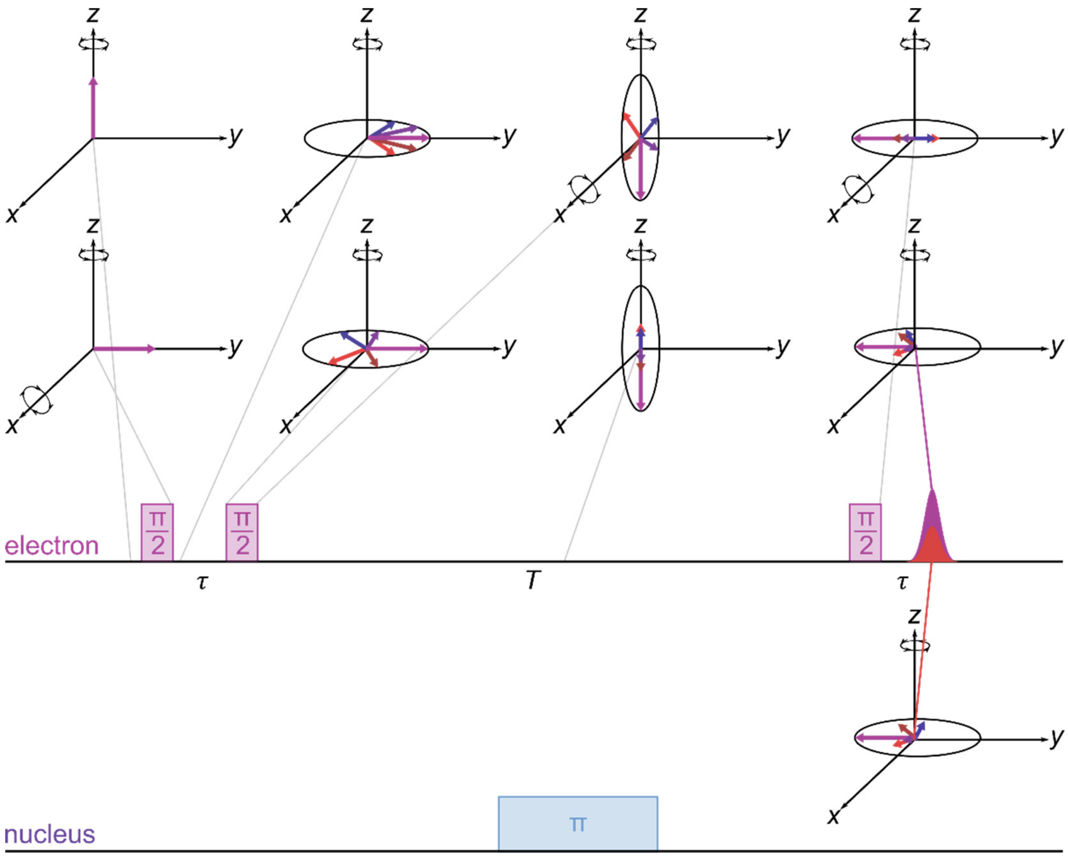

Figure 3. A depiction of the bulk magnetization throughout the Mims ENDOR pulse sequence. The magnetization is presented in a frame rotating around the *z* axis at the central frequency of the excitation pulse bandwidth. Prior to the first pulse the magnetization is aligned along the *z* axis. The first pulse rotates the magnetization down to the *xy* plane. The electrons with resonance frequencies larger or smaller than the excitation pulse frequency precess faster (blue tinted) or slower (red tinted) relative to the electrons that are directly resonant with the excitation pulse. During the time τ between the first two pulses the magnetization spreads around the *xy* plane. The second pulse rotates the plane of magnetization from the *xy* plane to the *xz* plane. The magnetization in the *xy* plane is averaged out or decays during the long period *T* so only the *z* axis magnetization remains. The final pulse rotates the *xz* plane back to the *xy* plane and the remaining *z* component magnetization once again precesses around the *xy* plane. At the time τ after the final pulse, the magnetization is directed primarily in one direction generating a stimulated echo (purple echo). A radio frequency (RF) pulse that is resonant with a magnetic nucleus during the pulse sequence will alter the resonant frequency of electrons coupled to the nucleus (blue magnetization vector) which will not refocus to be part of the stimulated echo, decreasing the echo intensity (red echo).

The reason that the Mims ENDOR sequence is sub-optimal for larger hyperfine couplings is due to an additional effect of the stimulated echo. The first two π/2 pulses generate a “polarization grating”, which is a sinusoidal subset of electron resonance frequencies that are stored along the z-axis during *T*. The polarization grating spacing is a function of τ (increased τ yields narrower spacing), and it leads to a τ-dependent suppression envelope (with maximum suppression at frequencies $n/2\tau, n = 0, \pm1, \pm2, \ldots$) across the ENDOR spectrum. An example of the suppression envelope is shown in Figure 4.

The ENDOR experiment is ideal for measuring hyperfine couplings. For an electron spin center and nucleus (both assumed spin 1/2) the ENDOR spectrum will contain two features located approximately symmetric around the Larmor frequency of the nucleus. The central and splitting frequency of ENDOR spectra are dependent upon the magnitude of hyperfine coupling relative to the nuclear Zeeman coupling. The protons in this work all have hyperfine couplings less than 3 MHz which when compared to the nuclear Zeeman coupling ≈ 15 MHz the protons are all well within the weak coupling regime. Functionally this means that the ENDOR spectra in this work are symmetrically centered around the nuclear Zeeman frequency and split by the magnitude of the hyperfine coupling.

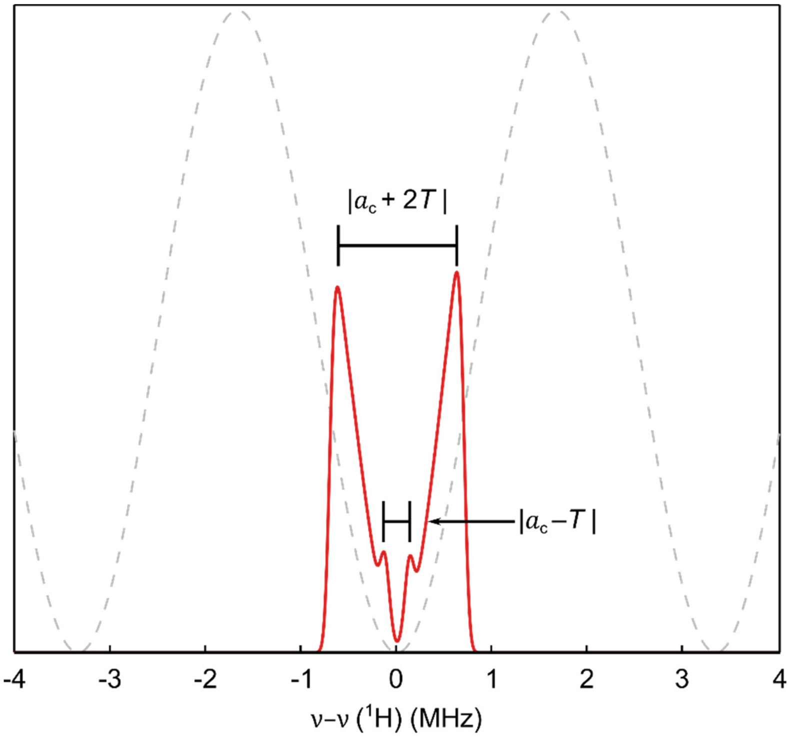

Figure 4. A simulation of a Mims ENDOR spectrum for a proton weakly coupled to a spin-1/2 electron. The contact coupling is 0.28 MHz, and the dipolar coupling is 0.56 MHz. The gray dashed line is the Mims suppression envelope for a τ of 150 ns. The suppression due to $n = \pm1$ is at $\approx \pm3.3$ MHz.

As described above, the hyperfine coupling can be broken apart into two components. The contact coupling is orientation independent. The dipolar coupling on the other hand is dependent upon the distance between the spin center and a given nucleus and their orientation to the applied magnetic field. These orientation dependent interactions contain valuable structural information that can be extracted through careful analysis.

Traditionally, measuring orientation dependent interactions requires measuring single crystals, or making single-molecule measurements. There is an additional method of measuring orientation dependent interactions for certain spin centers with EPR that doesn't require growing crystals or single molecule measurements.

When a disordered solid (either a sample frozen in solvent, or an amorphous solid) EPR sample is placed within an applied magnetic field, the orientations of the spin centers (molecules) remain stationary. The unpaired spins on the other hand are mobile and align along the applied magnetic field as described above. As the electrons align with the magnetic field, they probe the of orientations of the stochastically disordered spin centers. A simple diagram of this effect is shown in Figure 5 on the left.

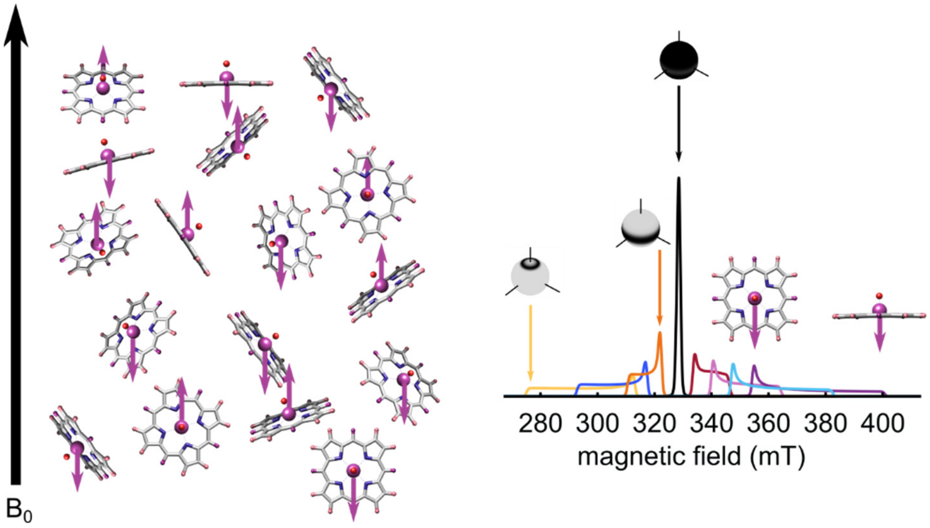

Figure 5. In frozen solution, or a magnetically dilute amorphous solid, the paramagnetic centers are stochastically disordered. The unpaired electrons are aligned preferentially with an applied magnetic field. Electron magnetic moments tend towards aligning preferentially along the field; however, for ease of visualization they are depicted as purely parallel or antiparallel in the figure. Measured parameters are a function of the orientation of each given molecule relative to the magnetic field. The experimentally acquired spectrum is the sum over all the spectra from all molecular orientations. The field positions that result in limited, perpendicular and parallel orientation selection in a vanadyl porphyrin system are highlighted on the right.

As described above, the distribution of frequencies that unpaired electrons resonate with is often much larger than the excitation bandwidth of a given pulse (and resonator). A given pulse only interacts with the subset of unpaired electrons whose resonance frequencies lie within the pulse excitation band. When the resonance frequency of the electron spins is dependent on the molecular orientation relative to the external field, the excitation pulse necessarily becomes orientation dependent. For certain spin centers it becomes possible to generate orientation-dependent spectra that provide more complete information about the magnetic interactions of the spin center.

The dominant interaction in vanadyl porphyrins (see below) is the hyperfine coupling between the unpaired electron on the vanadyl ion and the 51-vanadium nucleus (>99% natural abundance). This hyperfine interaction is strongly anisotropic due to the fact that the electron is located in a d-orbital centered on the nucleus. By selecting combinations of magnetic field and microwave frequencies, orientation- and transition-dependent measurements can be made. The selection of three such field positions are shown in Figure 5 on the right.

The vanadium hyperfine tensor is axial (see Table 1 at the end of Section 3.3 for values), and the orientation dependence of the effective hyperfine coupling is described by

$$A(\theta) = \sqrt{{A_{\perp}}^2 \sin^2\theta + {A_{\parallel}}^2 \cos^2\theta} \tag{7}$$

where $A_{\perp}$ and $A_{\parallel}$ are the perpendicular and parallel values of the hyperfine tensor respectively and θ is the angle between the symmetry axis of the hyperfine tensor (along $A_{\parallel}$, which is along the axis normal to the porphyrin plane) and the external magnetic field. The anisotropy of the *g*-tensor ($g_{\perp}$ = 1.984, $g_{\parallel}$ = 1.964) is negligible because at X-band frequencies used in this work it is much smaller than the hyperfine anisotropy. The angular dependence of the resonance positions is primarily due to hyperfine anisotropy at X-band frequencies.

The resonance fields of an arbitrary interaction tensor are determined by the orientation of the interaction tensor relative to the external field. In order to simulate an EPR spectrum, the interaction tensors and the magnetic field need to be expressed in the same frame. In practice, the mechanics of this process involve defining an interaction tensor in the molecular frame by applying a frame transformation

$$\boldsymbol{A}_{\mathrm{M}} = \boldsymbol{R}\boldsymbol{A}_{\mathrm{T}}\boldsymbol{R}^{\mathrm{T}} \tag{8}$$

where $\boldsymbol{A}_{\mathrm{M}}$ and $\boldsymbol{A}_{\mathrm{T}}$ are the tensor in the molecular frame and tensor frame respectively. The rotation matrix ***R*** can be written as a product of three rotations around conventional axes. In the *zyz* convention (as used in this work) ***R*** is defined by

$$\boldsymbol{R} = \boldsymbol{R}_{z''}(\gamma)\boldsymbol{R}_{y'}(\beta)\boldsymbol{R}_{z}(\alpha) \tag{9}$$

where each $\boldsymbol{R}_i(j)$ is a rotation matrix describing a rotation by an angle j around the axis *i.* Explicitly, this describes a rotation around the original z axis, followed by a rotation around the new y axis, and finally a rotation around the resulting z axis.

The molecular frame is defined by the axial vanadium hyperfine tensor for the simulations presented below. The rotation angles for proton hyperfine coupling tensors were treated as fitting parameters (see Table 1 at the end of Section 3.3) for the simulations.

CHAPTER 2: VANADYL PORPHYRINS IN OIL

Abstract:

This chapter describes why the petroleum industry has an interest in vanadium compounds and the chemical environment surrounding them. A brief overview of the last 80 years of vanadium compound crude-oil research is included to frame the current state of research into this area. Additionally, a description of a new method of vanadium compound research involving the combination of high-resolution ENDOR and numerical analysis is introduced.

2.1 THE EFFECT OF VANADYL PORPHYRINS IN CRUDE OIL REFINING

The petroleum industry refines billions of barrels of crude oil annually. An important step in crude oil refining is catalytic hydrotreating; the removal or deactivation of contaminants that interfere with the burning of fuel.[5] One of the most common catalytic surfaces in hydrodesulfurization is MoS_2; through scanning tunneling microscopy and calculations multiple catalytic pathways are understood to exist.[6] One example pathway demonstrating the hydrogenation of a thiol is depicted in Figure 6. A “hole” in the surface of MoS_2 creates a potential well for the thiol functional group. Hydrogen gas is pumped in along with the unrefined oil and breaks the thiol bond forming hydrogen sulfide and the hydrogenated original molecule. Unfortunately, in the process of hydrotreating, catalysts are deactivated by a buildup of coke and metal deposition. This effect was first published in 1950,[7] and in the decades since there has been ongoing research to understand the interaction between crude oil and the refinery catalysts. [8–11] One particularly problematic issue is the deposition of vanadium; quantities as low as 2% of the total mass built up on the catalyst can result in a 50% loss in catalytic activity.[5,12] Essentially all vanadium compounds (and other trace metals) are located within the densest layers of crude oil such as the asphaltene, bitumen and vacuum residual layers. In practice, oil refineries focus upon refining the less dense (and therefore less likely to contain catalytic poisoning compounds) layers of oil. However, as crude oil is a finite resource there is great interest in the removal of vanadium (and other trace metals) to increase the value of the dense, previously unrefined oil.[12–25]

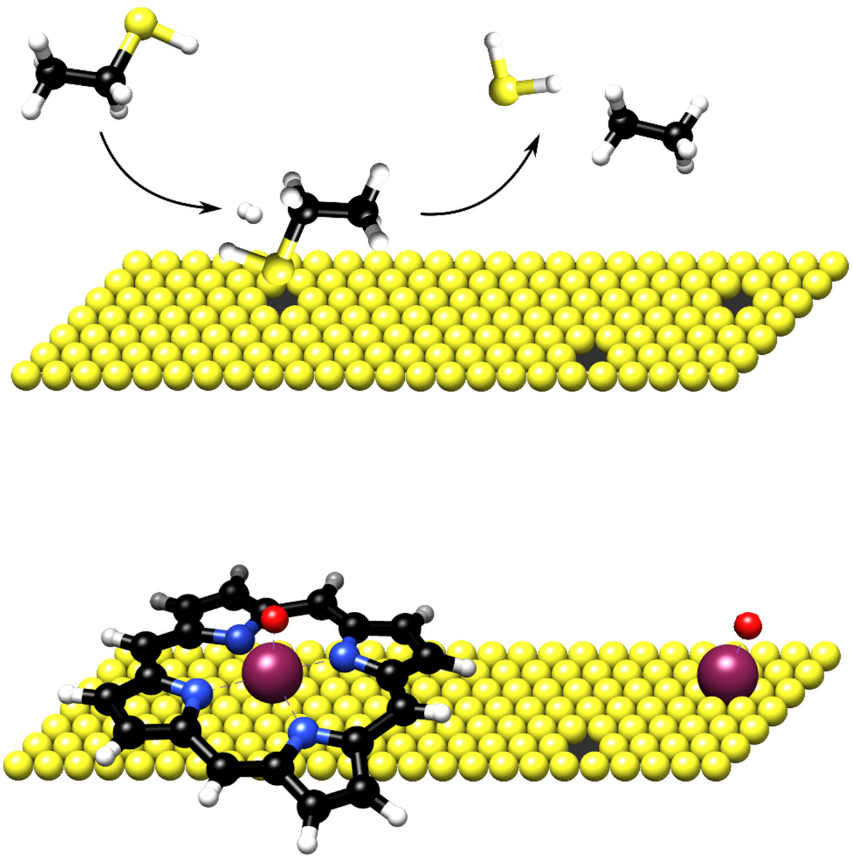

Figure 6. The catalytic surface of MoS_2.. The top figure displays an example catalytic hydrogenation. The thiol group on ethanethiol is attracted to holes in the MoS_2 surface. The thiol bond is broken and nearby hydrogen binds to form hydrogen sulfide and ethane. The bottom figure shows the binding of vanadyl porphyrins and vanadyl ions. The vanadyl ions are bound tightly to the surface and over time as more catalytic regions are blocked by vanadyl the catalyst efficiency decreases.

Vanadium (and other trace metal) compounds in crude oil tend to be in the densest layers. The concentration of vanadium in these petroleum layers varies from $\lesssim$10 ppm to $\gtrsim$1200 ppm, this can be a fingerprint of the age and source of the crude oil.[26] The separation of vanadium from these layers is non-trivial because these dense layers are challenging to work with. These layers of oil are insoluble in most solvents. Additionally, solvents that can dissolve heavy layers of oil often drive aggregation of the large molecular clusters that primarily make up these layers. Much of the vanadium is trapped within these aggregations, further complicating the separation.[27]

These heavy layers of crude oil are often considered to be less valuable due to increased cost of refining, primarily due to the increased metal concentration. A better understanding of vanadium compounds and their chemical environment in crude oil could lead to improved separation techniques or a better understanding of the geological formation or improvements in fingerprinting oil sources. Despite the difficulty in separating these compounds, there has been success in determining information about the nature of vanadium in asphaltenes and unprocessed crude oil.

2.2 ANALYSIS OF VANADYL COMPOUNDS IN CRUDE OIL

The discovery of vanadyl porphyrins, the primary chemical form of vanadium in crude oils is attributed to Treibs in 1936.[28] Interest in vanadyl porphyrins in general in crude oil has been an ongoing area of research ever since.[9,17,29] Initially this interest was from a geochemical perspective to develop a better understanding of the source of the porphyrins and the bound vanadium. The link between vanadium content and catalyst deactivation during refining was first described by Mills in 1950.[7] From that point on the research upon vanadyl porphyrins in crude oil focused primarily on separation[11], and interaction with catalytic surfaces[30] but geochemical research continued.[31]

Within the realm of geochemistry, the original source of crude oil can be determined through the concentration of nickel and vanadium. The overall concentration of these metals and their ratios are informative of the source of crude oil.[32] Crude oil from carbonate source rocks has a large (> 100 ppm) concentration of metals. Crude oil sourced from aqueous environments (fresh or salt water) tend to have lower (10-100 ppm) concentrations of metal. Crude oil with minimal (< 10 ppm) metal content is sourced from land-based plant debris. Further analysis can be made from the ratio of vanadium to nickel ([V]/[Ni]). In samples from fresh-water sources [V]/[Ni] is often greater than 1, reaching above 2 for some samples. Conversely, a lower [V]/[Ni] is linked to marine-sourced crude oil samples.[33] The age of crude oil sources is also tentatively linked to the ratio of nickel and vanadium although the evidence for this trend is not as robust as the evidence for source determination. The metal concentration appears to increase with the age of the source. Additionally, the [V]/[Ni] ratio increases with source age.[26,33]

The original source of vanadium in crude oil is attributed primarily to biogenesis.[21,28] As porphyrin-containing cells are trapped in petroleum forming conditions, the porphyrin frame remains relatively stable. Over geologic time, the magnesium and iron from chlorophyll and hemoglobin (the two largest contributors to metallated porphyrins) respectively are exchanged with the more stable vanadyl and nickel found in trace quantities in most life.[32] The basic porphyrin frames of chlorophyll and hemoglobin are similar to the most commonly found porphyrin structures in crude oil (see Figure 7) which is further support for the biogenesis hypothesis of vanadyl porphyrins in crude oil.

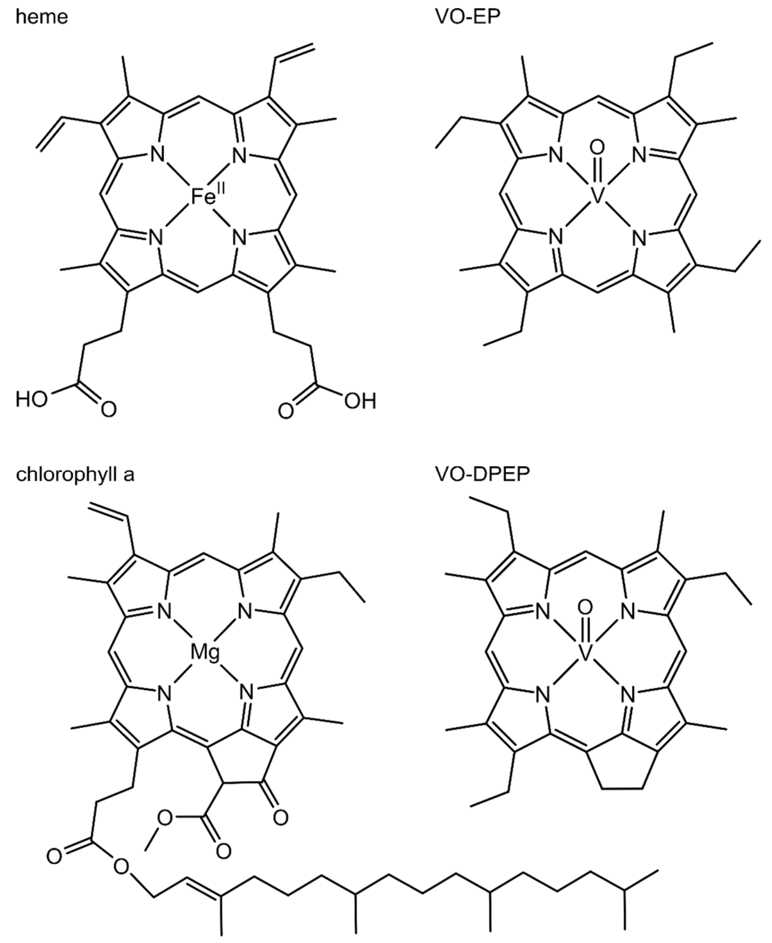

Figure 7. The biogenic hypothesis is the leading hypothesis of the formation of vanadyl porphyrins in crude oil. The most common porphyrins, heme and chlorophyll, are altered over geologic time to form vanadyl porphyrins. Vanadyl etioporphyrin (VO-EP) and vanadyl deoxophylloerythroetioporphyrin (VO-DPEP) are the primary vanadyl porphyrins formed, and the other vanadyl porphyrins are derived from further chemical changes over time.

The abundance of individual porphyrin species is also a signature of age.[32] The primary method of contemporary petroleomics is Fourier Transform Ion Cyclotron Mass Spectrometry (FT-ICR MS). This high-resolution mass spectrometry technique can resolve *m/z* differences on the order of a mDa (≈ a single electron mass).[34] Through FT-ICR MS hundreds of individual vanadyl containing molecules have been identified. Combined with other spectroscopic data (see below) many of these can be assigned primarily to different vanadyl porphyrins. The most common vanadyl porphyrins are vanadyl etioporphyrin (VO-EP), and vanadyl deoxophylloerythroetioporphyrin (VO-DPEP).[13] However, other vanadyl porphyrins such as vanadyl octaethylporphyrin (VO-OEP) and vanadyl rhodoporphyrin (VO-RP) also occur in a relative abundance. The link between age and ratio is attributed to the idea that over geologic time and energy the original biogenic porphyrins (primarily EP and DPEP) continue to go through various chemical reactions expanding or contracting the porphyrin ligand.

2.3 ELECTRONIC STRUCTURE OF VANADYL PORPHYRINS

The structure of vanadyl porphyrins is mostly answered by X-ray crystallography revealing that vanadium is primarily in in the form of vanadyl ions (VO^{2+}, consisting of V^{4+} and O^{2-}) connected to 4 nitrogens.[5] The first electronic structure calculation for the vanadyl ion was published in 1962.[35] The ion has an electron configuration of [Ar]$3d^1$ making vanadyl a spin-1/2 paramagnet. When ligated to a porphyrin, the vanadyl SOMO is primarily in a $3\mathrm{d}_{xy}$ like orbital with lobes pointing towards the meso porphyrin position in between the nitrogens and the unique *z*-axis defined by the V-O bond. The results of an example density functional theory (DFT) calculation of the SOMO in a vanadyl porphyrin is shown in Figure 8. The majority of the calculated Mulliken spin population is centered on the vanadyl ion, the remaining 0.05 spin population is distributed across the porphyrin ligand.

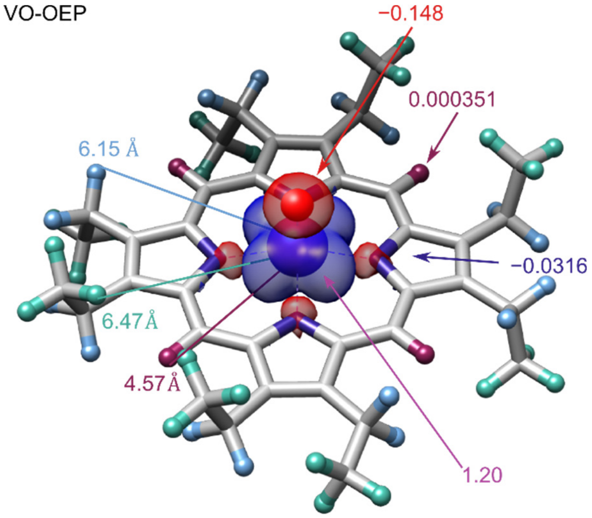

Figure 8. Calculated electron spin density of VO-OEP. The spin density contour level is drawn at ±0.002 electrons a_0^{-3}, and the positive and negative spin densities are colored blue and red, respectively. Values for magnetic nuclei with a Mulliken spin population >0.0001 and computationally predicted average values for vanadyl-proton distances are shown. Calculated distances from vanadium to selected protons are highlighted. The calculation was performed with ORCA 3.0.3 using B3LYP as the functional with EPR-II as the basis set for all atoms except vanadium which was assigned the CP(PPP) basis set.

The calculation of the vanadyl ion electronic structure assisted in the rationalization of the experimental parameters of the spin Hamiltonian measured through CW EPR. The spin Hamiltonian parameters of the vanadyl ion and vanadyl porphyrins are quite similar. The magnitude of the parameters vary with solvent interaction and ligation; however, the *g* and vanadium hyperfine tensors remain colinear and axial in every porphyrin system.[36,37] The interpretation of these experiments is that the unpaired electron centered on the vanadyl ion does not experience significantly different chemical environments as a function of varying the porphyrin ligand. However, there are measurable differences for certain changes to the porphyrin ligand. For example, including more electronegative atoms such as sulfur or oxygen in the porphyrin ring drives measurable shifts in EPR parameters.[38] As discussed below, traditional CW EPR does not have the resolution to differentiate smaller perturbations to the electronic structure of vanadyl porphyrins, but by utilizing pulse EPR methods, the required resolution is achievable.

2.4 MEASURING VANADYL IN SITU

The nature of crude oil is a complex mixture of organic molecules with a wide distribution of molecular weights that, as mentioned above, are a function of the age and original source of the crude oil. The low-density fractions are relatively easily removed for processing, but the remaining dense layers require more processing. These dense layers often include large macrocyclic compounds that are resistant to most solvents. Additionally, many solvents drive further aggregation within these layers.[39] Therefore, the development of separation methodology is necessarily complex.[16,40] It is crucial to improve the understanding of interaction between the vanadyl porphyrins and the surrounding chemical environment to further develop separation methodology. This understanding fundamentally requires measurement of vanadyl porphyrins in situ.

The interaction between vanadyl porphyrins and the surrounding environment can be subtly complex. For example, there are differences in the measured crude oil vanadyl porphyrin concentration between atomic absorption and UV/Vis.[18,41] Initially the difference in concentration led to speculation of a non-negligible concentration of non-porphyrin vanadyl or other forms of vanadium in crude oil. However, an effect (credited to the complex crude oil matrix) that suppresses the Soret band measured by UV/Vis has been described recently.[42] The Soret band suppression does not rule out the possibility of non-porphyrin vanadyl/vanadium, but it does highlight the complexity of the crude oil matrix.

As mentioned earlier the most common technique in contemporary petroleomics is FT-ICR MS. The earliest examples of measuring crude oil with FT-ICR MS utilized a preparatory chemical separation.[34] It was later shown that that diluting the crude oil sample was all the preparation required.[39,40] In spite of the separation-free approach, FT-ICR MS is a fundamentally destructive technique, and any information informative of the interaction between vanadyl porphyrins and the surrounding environment is lost.

A non-destructive experimental method that has been used successfully to measure aspects of crude oil in situ is magnetic resonance. Both EPR and NMR have been used to measure the approximate sizes of aggregated molecules in crude oil. The rotational correlation times of vanadyl porphyrins in crude oil are related to the amount of aggregation in the local chemical environment experienced by the vanadyl porphyrin, and CW EPR has been used to probe these rotational correlation times.[45,46] Similarly, the amount of molecular aggregation has an effect on the nuclear relaxation times, and NMR has been used to measure this effect yielding estimates of aggregation size.[47]

In addition to measuring the local environment within crude oil, magnetic resonance can be used to measure the interaction between the vanadyl ion and porphyrin ligand in situ. Through ENDOR spectroscopy, the interactions between the unpaired spin and the surrounding magnetic nuclei (hydrogen and nitrogen) have been measured in crude oil samples with no pre-processing.[48,49]

2.5 DEVELOPMENT OF A HIGH-RESOLUTION ENDOR ANALYSIS METHOD

Within vanadyl porphyrin research there is an opportunity for the development of a novel methodology. Through FT-ICR MS the structure of vanadyl porphyrins can be determined reasonably accurately. However, information about the local chemical environment is lost. Magnetic resonance is an experimental technique that allows measurement of crude oil samples in situ; therefore, the environmental interactions are preserved. EPR spectroscopy is a powerful experimental technique for the investigation of vanadyl porphyrins in crude oil. The advantage of using EPR for analysis of these complex spectra is that EPR is blind to diamagnetic compounds. As shown below, the only paramagnetic systems detectable within crude oil samples are vanadyl ions, and stable organic radicals. The stable organic radical feature is the most intense feature in the crude oil spectra shown in this work. However, despite the intensity of the feature the vanadyl signal is easily analyzed due to distinct differences in spectral width. Magnetic resonance and specifically EPR have been used to analyze vanadyl porphyrins since the late 1950's.[50] The primary usage has been through CW EPR, which is informative about many of the bulk properties of crude oil. However, as shown in this work, CW EPR is not capable of resolving small differences in the interaction of the unpaired electron on vanadyl ions and the magnetic nuclei on the porphyrin ligand. Pulse EPR techniques are capable of far higher resolution than CW EPR, and as shown in this work able to resolve differences between similar vanadyl porphyrin ligands. The contemporary work in magnetic resonance (mentioned above) has demonstrated the utility of measuring crude oil with pulse EPR. However, there is potentially more information within the data than can be extracted by a deeper numerical analysis. The work presented in this dissertation is describing efforts towards combining high-resolution ENDOR spectroscopy with numerical methods to better investigate vanadyl porphyrins in situ.

In the next chapter a complete analysis of the magnetic parameters of four model vanadyl porphyrins that either directly occur or simulate aspects of vanadyl porphyrins found in crude oil are presented. The analysis includes CW EPR, high-resolution ENDOR, X-ray diffraction, and DFT calculations. Despite the chemical similarity of these vanadyl porphyrins, high-resolution ENDOR measurements of the proton hyperfine couplings are differentiable. Additionally, quantitative analysis of mixtures of these model compounds demonstrate that the proton hyperfine couplings can quantify the amount of individual vanadyl porphyrins in more complex mixtures.

The final chapter investigates the vanadyl porphyrins in situ. A series of crude oil samples from domestic and international sources are measured with high-resolution ENDOR. The vanadyl porphyrin content from each crude oil is analyzed through Tikhonov regularization that constrains the ill-posed nature of the complex distribution of vanadyl porphyrins found in crude oil. Through this regularization method a more thorough analysis of vanadyl porphyrins in crude oil is available compared to simulation alone.

CHAPTER 3: MODEL COMPOUND ANALYSIS

Abstract

This chapter describes the experimental analysis of four model vanadyl porphyrin molecules using ^{1}H ENDOR spectroscopy. These molecules reflect or are chemically similar to naturally occurring vanadyl porphyrins in crude oil. A complete explanation for all spectral features is given for each molecule. Additionally, a quantitative measurement of vanadyl porphyrin mixtures is included. These results are published (*Energy Fuels* 2019, 33, 5, 4237–4243).[51]

3.1 MODEL VANADYL PORPHYRIN SELECTION

To begin studying the ligand structure of various vanadyl porphyrins, four model compounds are utilized. The structures, with color coded chemically unique protons are shown in Figure 9. All porphyrins have an identical porphin core and differ only in the alkylation or arylation substitution patterns. Vanadyl octaethylporphyrin (VO-OEP) and vanadyl etioporphyrin (VO-EP) are used because they are among the most common petroporphyrins. In these ligands, the pyrrole hydrogens are all substituted with ethyl groups or a mix of methyl and ethyl groups (OEP and EP respectively), but the hydrogens at the four meso positions are preserved. VO-DPEP (another common petroporphyrin) has substituents at some of the porphyrin meso positions, replacing the meso protons.[52] To model porphyrins with 0 and 2 meso protons, vanadyl tetraphenylporphyrin (VO-TPP) and vanadyl diphenylporphyrin (VO-DPP) are used respectively.

3.2 CW EPR ON MODEL VANADYL PORPHYRINS

As mentioned in the introduction, the vanadyl ion VO^{2+} is paramagnetic with total electron spin 1/2. The single unpaired electron is in a primarily $3d_{xy}$ orbital centered on the vanadyl ion, with its four lobes in the porphyrin plane and pointing toward the porphyrin meso carbons. CW EPR probes the coupling between the delocalized unpaired electron and surrounding magnetic nuclei. The low-temperature X-band (ca. 9.3 GHz) CW EPR spectrum for VO-OEP (black) along with a simulation (red) is shown in Figure 10 (top). The simulation parameters are listed in Table 1 at the end of Section 3.3. The *g*-tensor and vanadium hyperfine tensor in the simulation are collinear and axial. As the *g*-tensor is essentially isotropic relative to the hyperfine tensor, the spectral features are primarily determined by the strongly anisotropic hyperfine splittings due to the coupling between the unpaired electron and the magnetic ^{51}V nucleus (99.75% natural abundance) with a nuclear spin of $I = 7/2$. The $2I+1 = 8$ central features (for m_I values between -7/2 and +7/2) between 310 and 360 mT are due to porphyrins aligned such that the V–O direction is perpendicular (and the porphyrin plane is parallel) to the applied magnetic field. The splittings that appear on both the high- and low-field sides of the central lines correspond to molecules oriented such that the V–O direction is parallel (and the porphyrin plane is perpendicular) to the magnetic field. The spectra from the different vanadyl porphyrins are similar, to assist with visual comparison each of the spectra are aligned in the bottom of Figure 10, the intense central feature ($m_I = -1/2$) is removed from each spectrum to highlight the less intense non-central features.

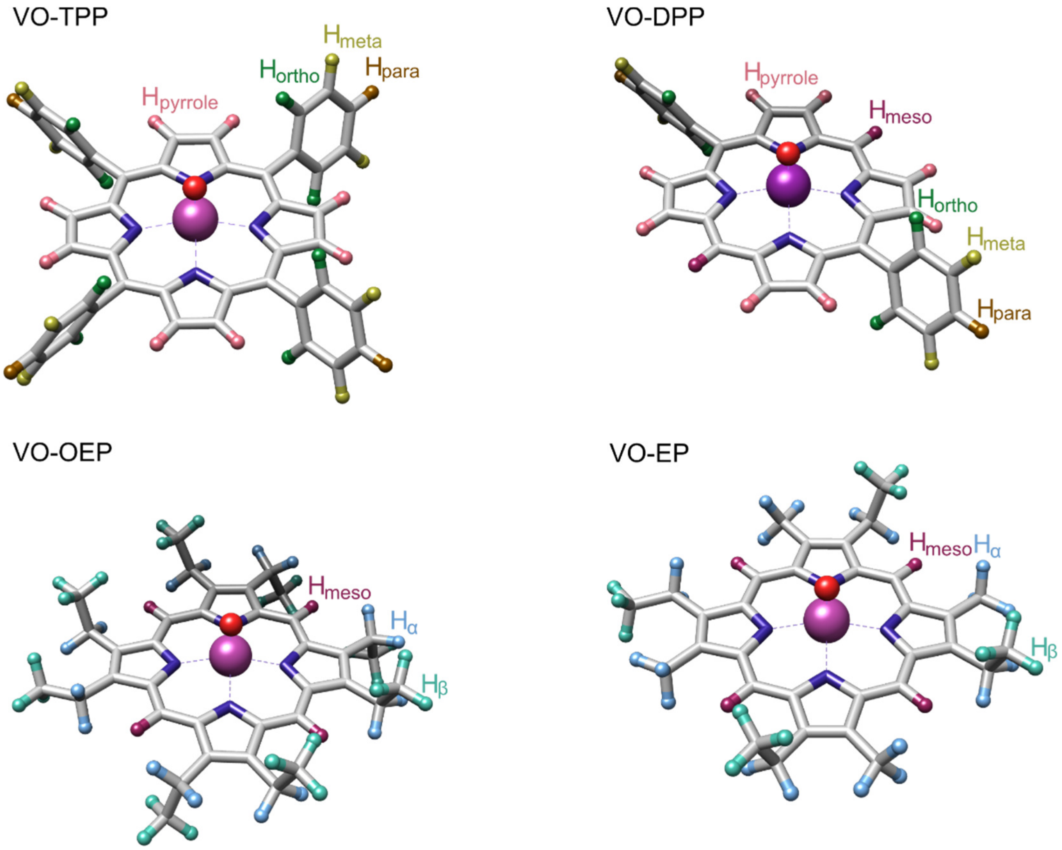

Figure 9. The four model vanadyl porphyrins analyzed in this chapter. The protons are colored by chemical identity and the coloring corresponds to the ENDOR spectral simulations discussed below. VO-EP and VO-OEP are common petroporphyrins, VO-TPP and VO-DPP are examples of porphyrins with less than four meso protons similar to VO-DPEP.

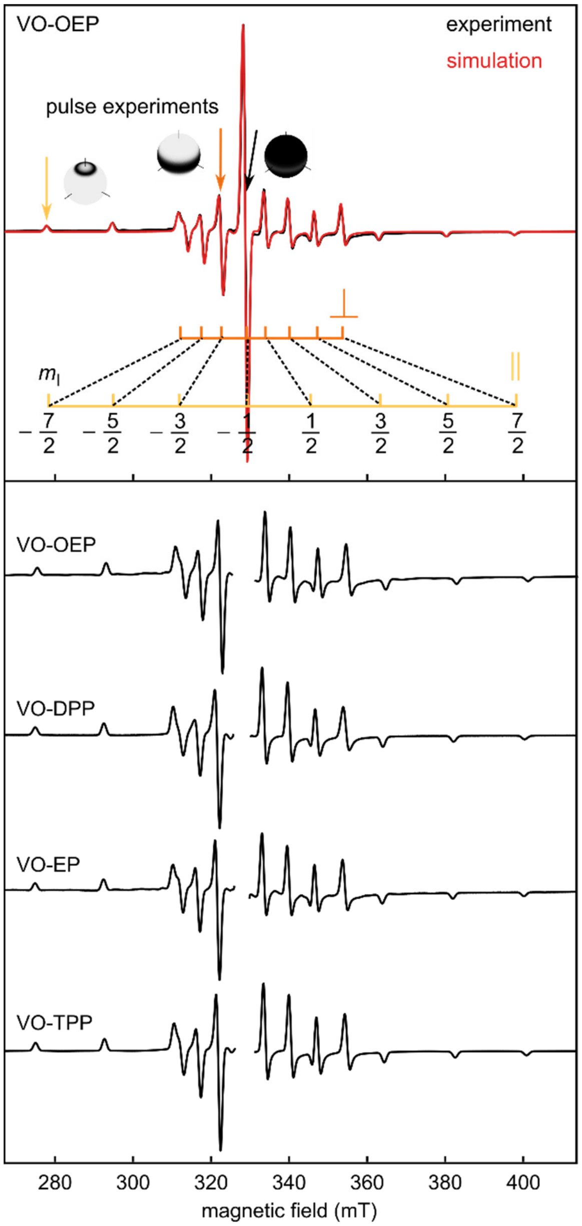

Figure 10. CW EPR spectra for the vanadyl porphyrin model compounds. Each compound was prepared by dissolving enough porphyrin into a 1:1 by volume mixture of deuterated chloroform and toluene to make a 1 mM solution. The samples were immediately frozen and stored in liquid nitrogen until measurement. Each porphyrin was measured between 107−110 K. The resonant frequency was ≈ 9.3 GHz for all compounds. The EPR spectrum (black) and spectral simulation (red) for VO-OEP are shown in the top panel. The parallel and perpendicular components of eight axial hyperfine features in yellow and orange respectively. The selected orientations for the ENDOR experiments are shown in the top of the figure. The dark regions on each sphere show the orientations that are excited by the respective pulse bandwidth. The CW EPR spectra for the other model compounds are in the bottom of the panel. The intense central $m_I = -1/2$ feature has been removed for ease of comparison of the less intense features.

The features measured with EPR can be assigned through simulation of the spin Hamiltonian parameters; the EPR simulations presented throughout this thesis are generated using the in-house developed MATLAB package EasySpin.[53] The eight overlaying nuclear manifolds are assigned, the features due to parallel and perpendicular edges of each manifold are highlighted in Figure 10. Three field positions with orientation dependence within a single nuclear manifold are also highlighted, measurement of those spectral regions yield single-crystal like spectra.

The CW EPR spectra for the other compounds shown in Figure 9 are essentially identical to that of VO-OEP within experimental noise. The similarity of the spectra indicates that the spin density distribution around the vanadyl ion is independent of the nature of the porphyrin and that the magnetic environment is mostly unperturbed by changes in the substitution pattern on the porphyrin ligand. The hyperfine couplings to the magnetic nuclei of the porphyrin ligand (protons and nitrogens) are unresolved; the features are “buried” in the broad spectral features due to the large anisotropic ^{51}V hyperfine coupling. Although CW EPR is useful for quantifying the amount of vanadium, it is incapable of differentiating vanadyl porphyrins. A technique with a higher resolution is required.

3.3 ENDOR ON MODEL VANADYL PORPHYRINS

As described in the introduction, ENDOR is a pulse EPR technique that measures the hyperfine coupling between magnetic nuclei and a paramagnetic center. The spectral location of features in ENDOR spectra are based upon the hyperfine coupling and the Larmor frequency of the magnetic nuclei. The ENDOR line shape position allows a full separation of features between the individual types of magnetic nuclei. The nuclei of interest (protons) are weakly coupled and therefore are centered around the proton Larmor frequency (ca. 15 MHz at 350 mT). Nitrogen signals are in the intermediate coupling regime, and cluster in the sub 6 MHz range, and vanadium is in the strongly coupled regime and the features are predicted to show up as a broad feature in the 50–250 MHz range. The orientation-selective ENDOR measurements are taken at different field values shown below. Each ENDOR spectrum is shifted by the proton Larmor frequency of the experimental field, this has the effect of centering each proton ENDOR spectrum at 0 MHz.

A potential limitation to the resolution of an ENDOR spectrum is the RF pulse bandwidth. For a rectangular pulse, the bandwidth is inversely proportional to the length, and the length of a given nutation angle is proportional to the square root of the applied power. Therefore, as the power of the applied RF increases, the bandwidth also increases. When the RF bandwidth is broader than the underlying line shape, a decrease in resolution is recorded. This effect is referred to as power broadening in the literature.[54]

Experimentally, a series of ENDOR spectra with varying RF pulse lengths demonstrates the effect of power broadening and informs the choice of the optimal pulse length. This series is shown in Figure 11. The resolution is no longer effected by pulse length with pulses ≥ 30 µs. The underlying spectral resolution is a function of overlapping spectral features, and the variations in coupling magnitude due to the distribution of the ensemble of magnetic nuclei.

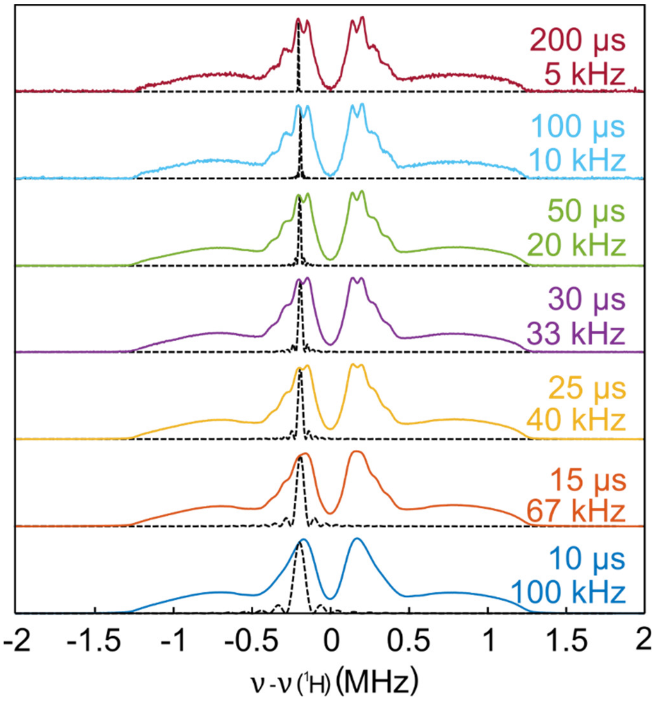

Figure 11. The effect of RF pulse length on the ENDOR spectrum of VO-OEP. The experimental results, pulse length and approximate pulse bandwidth are shown in color. A simulation of the RF pulse for each pulse length is shown as a dotted black line for each pulse length. Shorter RF pulses have increased bandwidth that can decrease resolution. Longer pulses yield a decrease in signal-to-noise per acquisition. The ideal pulse length for the ENDOR spectra in this work was determined to be 30 µs.

There are three ENDOR spectra for each model compound. The spectra correspond to the three positions highlighted in the CW EPR section. The ENDOR spectra collected at the peak of the −1/2 transition measures essentially the entire proton ENDOR spectrum. The *xy* peak of the −3/2 transition excites molecules with orientations where the components of the proton hyperfine tensor are parallel to the porphyrin plane. The *z* peak of the −7/2 transition excites the components of the protons aligned parallel to the VO bond. Assignment of proton features is made through a global fit of a simulation of the components in the three ENDOR spectra for each pure compound. The simulations were made with EasySpin[53] by simulating spectra for individual protons at three different measurement orientations and summing the individual spectra together.

All features in the experimental spectra can be rationalized by comparison to the proton assignments in the simulation. The distinguishing features of the ENDOR spectra are primarily due to the dipolar couplings T which are proportional to the inverse cube of the distance r between the proton and the unpaired electron spin density on the vanadium ion (see Equation (4) and Figure 2).

The hyperfine splitting with the largest magnitude is assigned to the meso protons. The associated spectral features are present in all spectra of compounds with meso protons (VO-DPP, VO-EP, VO-OEP) and are absent in VO-TPP, which does not have meso protons. The magnitude of the coupling is due to both through-space interactions and contact coupling. The meso proton is the closest proton to the unpaired electron and therefore has the largest through-space coupling (0.81 MHz, see Table 1). There is an additional 0.5 MHz contact coupling due to electron spin density directly at the location of the meso protons (see Figure 8). Additionally, DFT calculations (details below) support this assignment. The predicted through-space coupling is 0.86 MHz and contact coupling is 0.6 MHz.

The next-largest splitting is attributed to the pyrrole protons. The features attributed to the pyrrole protons appear in the spectra for VO-DPP and VO-TPP and are absent in the spectra for VO-EP and VO-OEP, supporting the assignment. The coupling consists of a 0.56 MHz through-space dipolar component and a 0.28 MHz contact contribution. These values are reduced relative to the meso proton because the pyrrole protons are further away ($r_{\mathrm{meso}} = 4.47(5)\,\text{Å}$, $r_{\mathrm{pyrrole}} = 5.2(4)\,\text{Å}$) from the vanadium ion and have a lower calculated electron spin density. The DFT calculations again support this assignment. Through-space coupling is calculated to be 0.56 MHz, and the calculated contact coupling is 0.24 MHz.

The next features assigned are the phenyl protons in VO-TPP and VO-DPP. These protons have no measurable contact coupling, and the dipolar couplings are smaller than those of the meso and pyrrole protons due to their increased distance from the vanadium. Additionally, based on crystal structures and geometry calculations, the porphyrin plane is slightly buckled breaking the symmetry, so the ortho and meta protons on either side of the phenyl rings have a different predicted coupling strength. Resolving the differences in ortho and meta hyperfine coupling is challenging. The separation of the features assigned to the ortho protons is near the resolution limit of the experiment. The simulation is closer to the experimental results if two different ortho features are assumed (single ortho spectrum not shown), but the meta protons are assigned to a single distance because spectral resolution is insufficient to support a two-component fit. Additionally, the resolution of the experiment does not allow assigning features from the para protons. DFT predicts $T \approx 0.1$ MHz for them. The associated features lie very close to the Larmor frequency, and this region of the spectrum is strongly suppressed due to the Mims suppression envelope (see Figure 4).

The final two types of protons are the alkyl protons in the methyl (α protons) and ethyl (α and β protons) groups in VO-OEP and VO-EP. Due to the distribution of dihedral angles in the ethyl and methyl groups, the α and β protons have overlapping distance distributions (relative to the vanadyl ion), which leads to similar hyperfine couplings. Unfortunately, due to this distribution overlap, the assignment of α or β protons remains ambiguous. The simulation instead includes three distinct alkyl proton features, that successfully model the features assigned to the α and β protons. Despite the overlap, the number and types of protons leads to qualitative differences in the alkyl region of the spectra of VO-OEP and VO-EP.

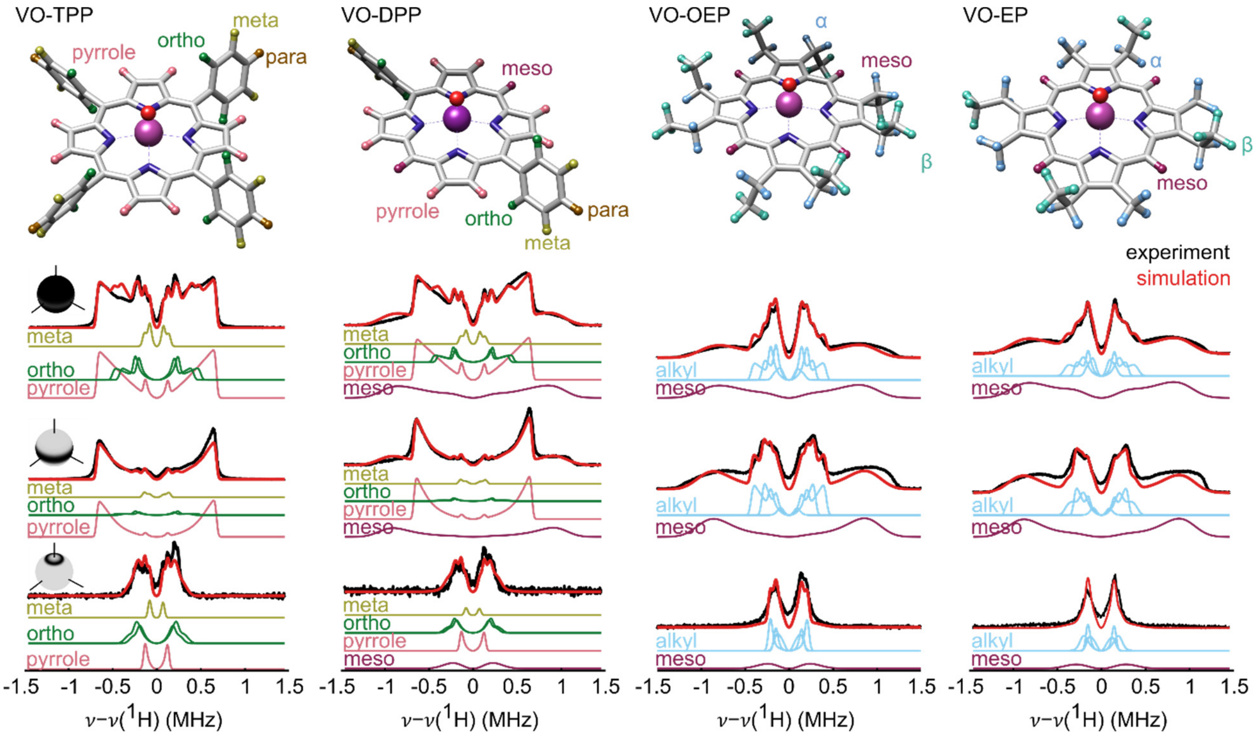

Figure 12. The ENDOR spectra for each model compound at the three orientations highlighted in Figure 10. The top depicts the four model compounds with the proton coloring to reflect the simulation assignments below. Each panel is the experimental ENDOR spectrum (black), and the overall simulation (red). Each simulation is constructed from a sum of individual spectra highlighted below a given simulation. The colors of individual simulations correspond to the assignment of protons in the structure above. Each column has ENDOR spectra all orientations (top), perpendicular orientations (middle), and parallel orientations (bottom).

The presence or absence of spectral features in the ENDOR spectra in Figure 12 allow classification of the porphyrin ligand. The most obvious features to assign are the protons directly attached to the porphyrin ring. The meso and pyrrole protons have unique and distinguishable spectra that do not completely overlap with the spectra from the protons on the alkyl substituents. Therefore, presence/absence of meso or pyrrole protons is immediately clear from the ENDOR spectra, allowing the identification of the ring substitution pattern. For example, comparing the spectra for VO-TPP and VO-OEP, the absence of meso protons in VO-TPP result in a spectrum that is ≈ 1 MHz narrower and does not feature broad peaks at ± 1 MHz. Without a pyrrole feature, the overall VO-OEP spectrum does not narrow, but the intense features at ± 0.7 MHz disappear. The ligand protons are not directly quantifiable; however, some semi-quantitative statements can be made. Comparing the intensities of the lines from the substituent protons to the ones from the porphyrin ring protons offers some insight into the number of protons in the alkyl or aryl substituents. For example, by comparing VO-OEP and VO-EP, the intensity of the central features relative to the meso wings reveals that VO-OEP has a larger number of weakly coupled ligand protons than VO-EP.

In order to support the analysis of high-resolution ENDOR, further experimental structural information was gathered through X-ray diffraction; additionally, predictions of structural and magnetic properties for each model compound were made through electronic structure calculations. The crystal structures for VO-OEP[55] and VO-EP[56] were available in the literature. Crystal structures for VO-TPP and VO-DPP grown through slow-evaporation in THF are presented in this dissertation. The X-ray data presented below was acquired with a Bruker Apex II single crystal X-ray diffractometer at -173 °C with a Mo tube. Computational predictions were performed with the package ORCA 4.1.1.[57] Each structure's geometry was optimized using the BP86[58] functional and D3BJ[59,60] dispersion correction with def-svp[61] and def-svp/j[62] basis sets. The integration grid and convergence criteria were set to 3 and tight, respectively. The predicted magnetic parameters for each model compound was calculated with the B3LYP[58,63–66] functional and EPR-II[67] basis set, an additional CP(PPP)[68] basis set was applied to the vanadium to better represent the electron density on the central metal atom. The integration grid and convergence criteria were set to 5 and tight, respectively.

The ENDOR results yield an experimental measurement of the distances of ligand protons from the vanadyl ion via dipolar couplings. A comparison of the ENDOR results with distances based on DFT calculations and experimental distances from crystal structures of vanadyl porphyrin compounds is shown in Figure 13. As demonstrated in the figure, ENDOR successfully captures the distribution of protons that are located between 4.5 – 8 Å from the vanadyl Ion. Even at the low-distance end of this range it appears that the point-dipole approximation (i.e. assuming the SOMO spin population on vanadyl to be localized at the vanadium nucleus) is reasonably accurate. The calculated value of T for meso and pyrrole protons is 0.88 MHz and 0.56 MHz respectively. The point-dipole approximation predicts 0.87 MHz and 0.53 MHz. The accuracy of the point-dipole approximation decreases along with the nucleus' distance from the vanadium as expected. For higher accuracy, the spatial extent of the SOMO must be taken into account more explicitly near this short-distance limit. The long-distance limit of about 8 Å is primarily due to a lack of spectral resolution and the low intensity due to the Mims ENDOR suppression envelope. The protons in the most common petroporphyrins fall within the 4.5 – 8 Å distance range accessible by high-resolution ENDOR.

Table 1. Simulation parameters for the model VO-porphyrins

Nucleus	Principal value 1 MHz	Principal value 2 MHz	Principal value 3 MHz
g-tensor	1.984(2)[a]	1.984(2)[a]	1.964(2)[a]
Atom	Hyperfine (MHz)		
^{51}V[b]	158(3)	158(3)	472(3)
	Dipolar (T)	Contact (a_c)	Frame ($[\alpha,\beta,\gamma]$) °
H meso[c]	0.8(3)	0.5(3)	[0, 90(5), 0]
H pyrrole[c]	0.56(4)	0.28(4)	[0, 90(5), 0]
H ortho $_{close}$[c,d]	0.47(7)	-	[0, 55(10), 0]
H ortho $_{far}$[c,d]	0.43(5)	-	[0, 55(10), 0]
H meta[c,d]	0.16(2)	-	[0, 90(10), 0]
H alkyl 1[c,d]	0.43(8)	-	[0, 60(15), 0]
H alkyl 2[c,d]	0.32(5)	-	[0, 80(15), 0]
H alkyl 3[c,d]	0.17(3)	-	[0, 45(15), 0]

a. *g*-tensor principal values are dimension-less

b. determined through CW EPR

c. determined through ^{1}H ENDOR

d. assumed purely dipolar (no contact term)

3.4 ENDOR ON MIXTURES OF MODEL VANADYL PORPHYRINS

The significant differences among the observed ENDOR spectra of vanadyl porphyrins suggest that it could be possible to differentiate them within mixtures. Mixtures of VO-EP/VO-OEP and of VO-TPP/VO-OEP were chosen to reflect the largest spectral similarity and difference respectively. An ENDOR spectrum at the -1/2 (limited orientation selection position) was measured for each solution. Then using linear combinations of pure-compound spectra, mixture mole fractions were determined through least-squares fitting. The results are shown in Figure 14. The error bars represent one standard deviation of the best-fit parameter. The difference in magnitude of the error bars is directly related to the relative differences of the pure-compound spectra. The ENDOR spectra of VO-OEP and VO-EP are very similar; therefore, as the relative concentration between the two compounds change, the overall spectrum does not significantly change. On the other hand, the spectral difference between VO-OEP and VO-TPP is more significant.

For example, as the relative concentration of VO-TPP increases, the spectral features due to the pyrrole protons becomes more intense and simultaneously the features due to meso protons decrease. These larger differences lead to a smaller uncertainty in the fitted parameters. Figure 14 shows that it is possible to determine the composition of porphyrins in a binary mixture with reasonable accuracy and precision. Remarkably, even vanadyl porphyrins as similar as VO-OEP and VO-EP are quantitatively distinguishable within a mixture.

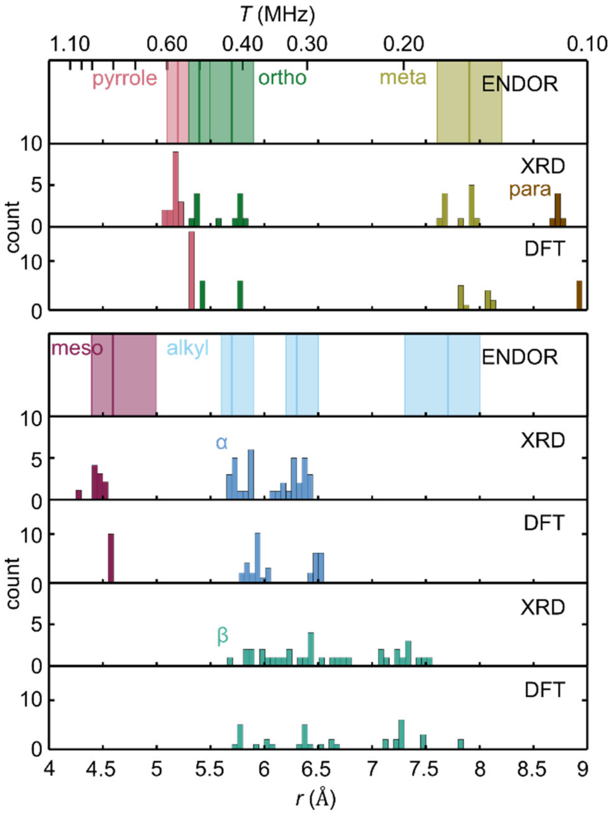

Figure 13. Distances calculated through experimental ENDOR data of the model vanadyl porphyrins for individual proton identities is shown with error bars. The distance distributions of protons as measured by X-ray diffraction and calculated through DFT is shown for comparison. The top axis includes the magnitude of the dipolar coupling and highlights the r^{-3} dependence.

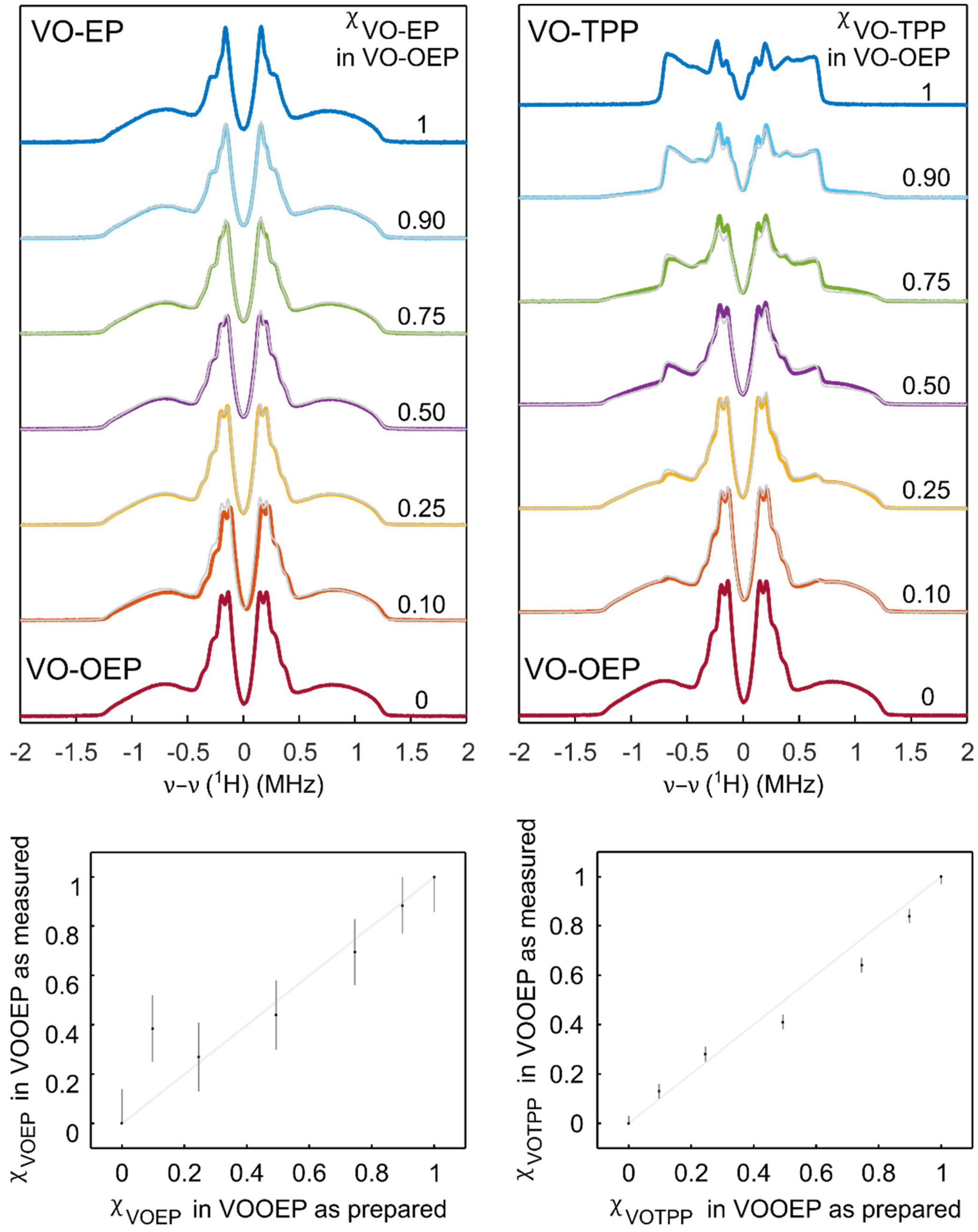

Figure 14. ENDOR spectra and analysis for each prepared mixture. The top two panels show mixtures of VO-EP/VO-OEP and VO-TPP/VO-OEP (left and right, respectively). Both panels show the spectra measured as the mole fraction of components changed as written. The “expected” spectrum calculated from an analytic sum of the pure spectra is shown in gray for each mixture. The bottom panels show the minimum and standard deviation of the best fit parameter from least-squares fitting for each mixture.

These positive results with model vanadyl porphyrin compounds lead directly into the next chapter: The measurement and analysis of crude oil samples. Crude oil samples include matrix protons as well as protons from ligands axially coordinated to V. They are therefore more complicated than the simple binary mixtures. However, even in complex mixtures, the ENDOR methodology outlined here will still be able to measure ring substitution pattern and relative content in ring and substituent protons, allowing a broad classification of porphyrin ligands.

CHAPTER 4: ANALYSIS OF VANADYL PORPHYRINS IN CRUDE OIL

Abstract

This chapter contains the details of the measurement and analysis of vanadyl porphyrins in crude oil. An ensemble of crude oil samples from around the world are measured with ENDOR spectroscopy. A qualitative analysis of the resulting ENDOR spectra leads to the necessity of introducing numerical methods for quantitative analysis. Finally, this leads to the introduction of applying Tikhonov regularization to analyze the model vanadyl porphyrins and the more complicated crude oil samples.

4.1 CRUDE OIL MEASUREMENT

The positive results of the analysis of vanadyl porphyrins described in the previous chapter leads to the next step of this project, measuring crude oil vanadyl porphyrins in situ. The crude oil samples in this chapter are measured directly with no preparation beyond placement within a quartz EPR sample tube. This minimal preparation serves the dual purpose of maintaining the crude oil matrix surrounding vanadyl porphyrins during analysis and facilitating the previously stated goal of straightforward sample preparation for method development.

A selection of crude oil samples from foreign and domestic sources (see Figure 15) are used for this analysis. The domestic samples are sourced from Alaskan and Californian (San Joaquin Valley) wells. There are South American samples (Ecuadorian and Venezuelan) and three samples from the Middle East, a pair of samples from Saudi Arabia that differ in their density (light and medium) and an Iraqi-sourced crude. These samples and analysis serve as a proof of concept for the ENDOR-based full-matrix vanadyl petroporphyrin speciation methodology, but these techniques should be satisfactorily robust to be used for additional samples in the future.

Figure 15. World map containing markers for the crude oil sources for the samples in this work. The marker color is used throughout this chapter for to differentiate crude oil spectra.

There are two distinguishable features in the EPR spectra of these crude oil samples measured at 110 K: a broad signal indicative of vanadyl, and a sharp feature assigned to miscellaneous stable organic radicals. An example of the CW EPR spectrum of a crude oil sample (medium density Saudi Arabian) is shown in Figure 16.

4.2 QUALITATIVE ANALYSIS OF CRUDE OIL ENDOR SPECTRA

The CW spectra of the crude oils all have a feature due to organic radicals that overlap the vanadyl spectrum. As described above, the ENDOR experiment is performed at a chosen field value corresponding to a spectral area of interest. The overlapping signal from the organic radical limits the choice of field positions that ENDOR can be performed at (without introducing spectral features due to organic radicals). The field positions that measure specific orientations of the vanadyl porphyrin ENDOR features are separated from the organic radical position; therefore, the three orientations measured with ENDOR for the model compounds described in Chapter 3 can be used similarly for crude oil samples.

From a spin dynamics perspective, the ENDOR spectra of a given crude oil should be nearly symmetric; however, the experimental results contain a pronounced skewness with a higher intensity in the lower half of the spectra, particularly in the parallel orientation acquisition (see Figure 17). Potential reasons for this skewness are a non-uniform RF excitation power over the range of the spectra, a difference in the required magnetic field power over the length of the RF pulse to fully drive a π rotation in different protons resonating at different frequencies, and a selective saturation effect due to incomplete nuclear relaxation over the amount of time in between individual ENDOR acquisitions (≈ 3 ms).[69] The source of the skewness remains an open question for now; however, for the analysis provided here, we eliminate the asymmetry by taking the average of the spectra for each absolute value of frequency and then reflecting the resulting half spectrum over the 0 MHz line. Additionally, the signal-to-noise ratio of vanadyl porphyrins in crude oil is (unsurprisingly) reduced relative to the model compounds due to lower concentration of vanadyl in the oil samples. The orientation-selective measurements have an even greater reduced signal-to-noise ratio due to the smaller sub-ensemble of electrons that are measured while acquiring the ENDOR signal. A seven-point, second-order polynomial Savitzky–Golay filter is applied to both the parallel and perpendicular orientation spectra for all of the crude oil samples. The effect of symmetrizing and noise filtering the spectra are shown in Figure 17 on an example (medium-density Saudi Arabian) crude oil.

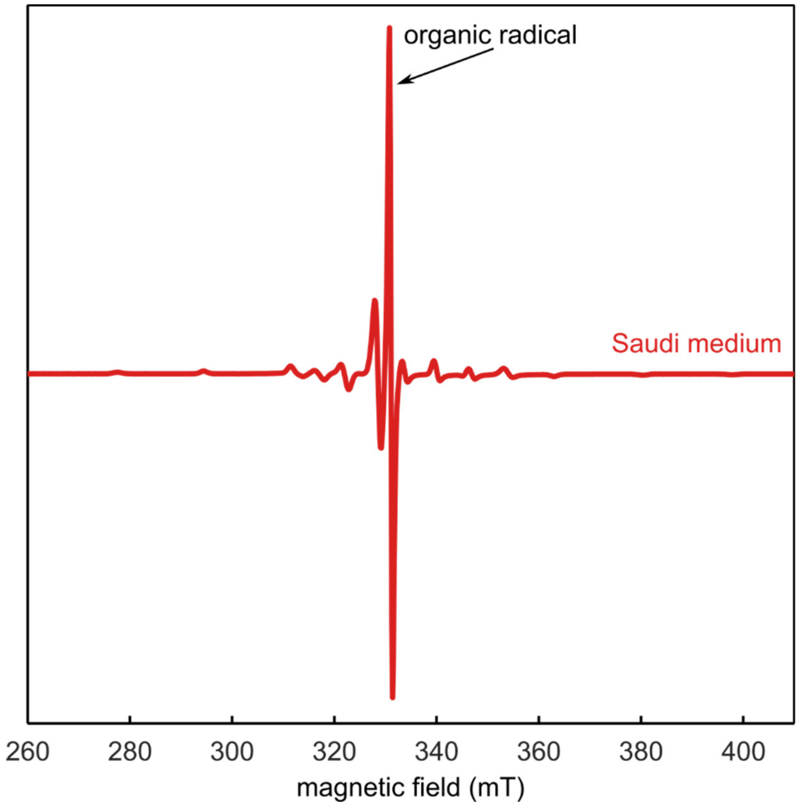

Figure 16. The CW EPR spectrum for medium density crude oil from Saudi Arabia. A sharp feature assigned to organic radicals overlaps the distinctive vanadyl spectrum. The EPR spectrum measured at 108 K with a microwave frequency of ≈ 9.3 GHz.

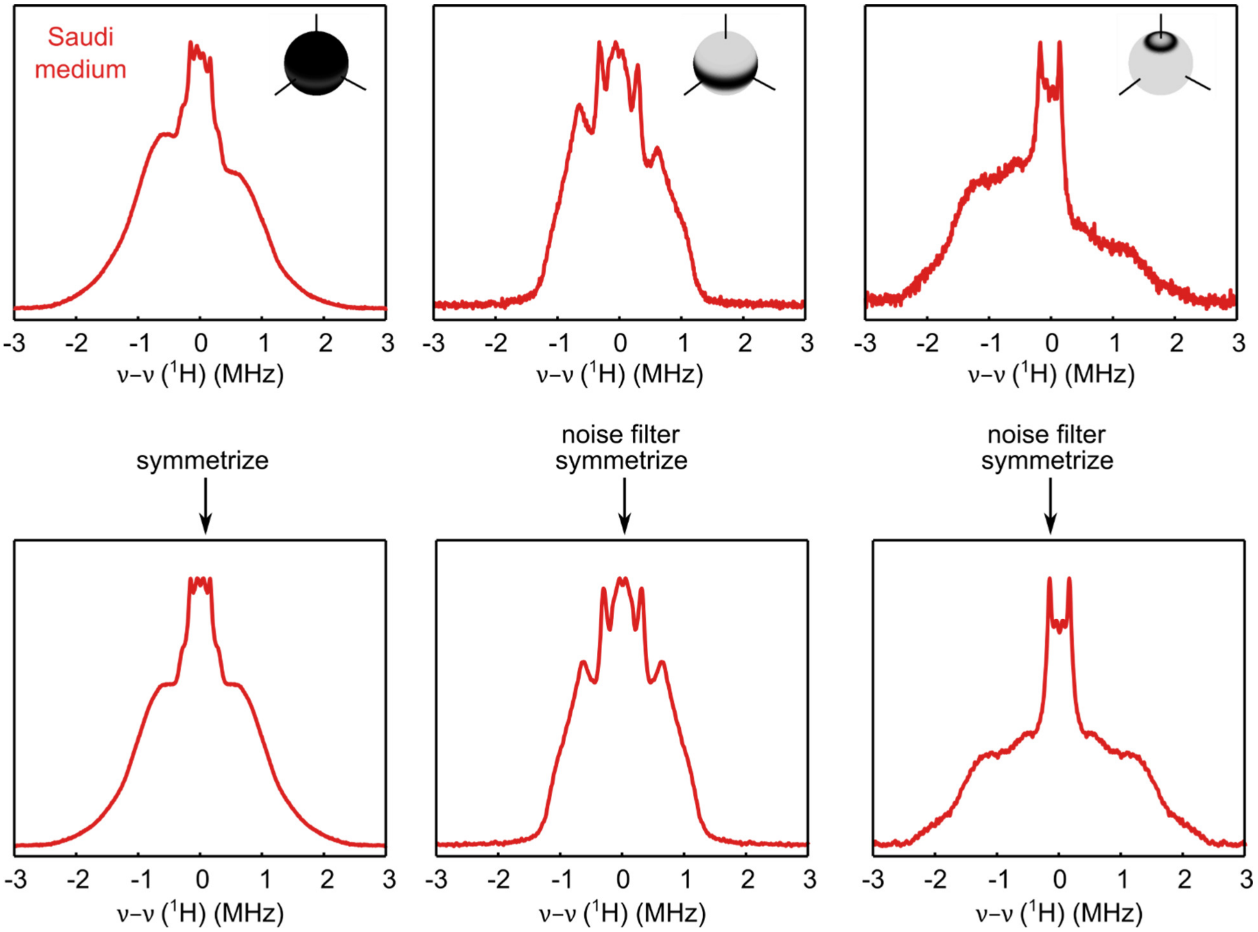

Figure 17. Crude-oil ENDOR spectra processing. Each ENDOR spectrum is symmetrized across 0 MHz, The perpendicular and parallel orientation spectra (center and right respectively) have an additional "noise-filtering" step by applying a Savitzky–Golay seven-point second-order filter to the symmetrized data.

The ENDOR spectra of all crude oils are quite similar, primarily because the vanadyl porphyrins contributing to the spectra are similar and the samples only differ by the relative abundance of different vanadyl porphyrin species. To improve visual distinction between the crude oil spectra, a "mean spectrum" is made by summing the individual crude oil spectra and dividing by the number of spectra. The mean spectrum is then subtracted from each individual spectrum. The residual spectra are informative of the intensity of given features compared to the average value in this ensemble of crude-oil samples.

The mean-subtracted ENDOR spectra shown in Figure 18 informs a mostly qualitative discussion about the distribution of vanadyl porphyrin protons in the individual crude oil samples. There are two main differences between the model compound and crude oil spectra: an increased intensity in the center (≈ 0 MHz) and on the outer wings (±≈2 MHz) of the crude oils relative to the model compound. The intensity at the center of the spectra is due to the increased concentration of matrix protons. The vanadyl porphyrins in crude oil are surrounded by a natural abundance of protons attached to the various organic molecules that make up the majority of the crude oil mixture. The unpaired electron on the vanadyl ion interacts with all the surrounding protons through dipolar coupling. Even with the effect of the Mims ENDOR suppression envelope (see Figure 4), the central region has significant intensity from the matrix protons. In contrast, matrix protons are absent in the samples of the model compounds studied in Chapter 3, since they were dissolved in perdeuterated solvents. The features at ±2 MHz are novel to the crude oil samples, as they are absent in the spectra of the model compounds. The magnitude of the hyperfine coupling responsible for these features is larger than the largest coupling (meso protons) measured in the model compounds; therefore, the protons coupled to the electron are either closer to the vanadyl, have increased electron density on the nucleus, or a combination of both. By combining a crystal structure of a vanadyl porphyrin with a solvent molecule coordinated axially to the vanadyl ion from beneath the porphyrin plane and the resulting DFT calculations (see below), these features are assigned to organic molecules in crude oil axially bound to the vanadyl ions.

Features rising above the base line for each spectrum suggest a larger amount of the protons assigned to those features (relative to the mean), and vice versa for features that fall below the base line. The largest deviation is in the sample from San Joaquin Valley, the increased intensity in the meso and axially bound region suggests there are more meso protons and protons on molecules coordinated to the vanadyl. Perhaps interestingly, the low-density Saudi sample has the opposite features, i.e. decreased meso and bottom bound protons, but there are not enough samples to make any conclusions of a trend between those features. The Venezuelan crude oil has the most intense alkyl features, this could potentially be supportive of a claim of higher concentrations of VO-EP and VO-OEP type porphyrins compared to the ringed porphyrins like VO-DPEP (see Figure 7). While it is possible to make educated guesses about the vanadyl porphyrin systems in crude oil based on the qualitative interpretation of these ENDOR spectra, particularly for larger differences, a more quantitative method is required to fully analyze the subtle differences contained within these spectra.

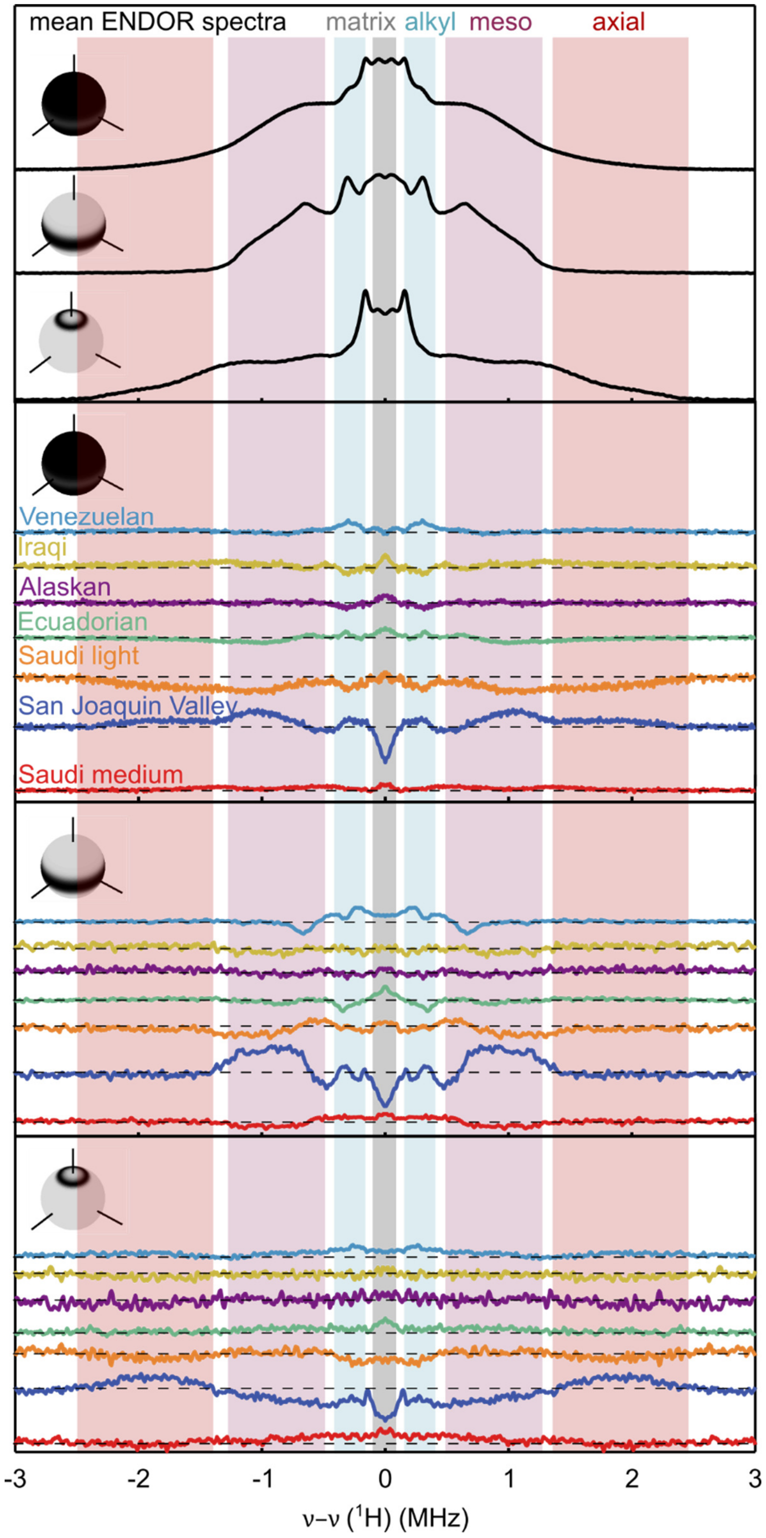

Figure 18. The mean subtracted crude oil ENDOR spectra. The top panel displays the mean spectrum for each orientation. The bottom three panels contain the ENDOR spectra minus the mean spectrum for each given orientation. The vertical columns highlight frequency ranges assigned to groups of protons.

4.3 NUMERICAL METHOD SELECTION

Each crude-oil ENDOR spectrum is composed of the sum of ENDOR spectra from all of individual species of vanadyl porphyrins in the crude oil. Furthermore, each individual vanadyl porphyrin spectrum is a sum of individual proton ENDOR spectra. The dimension of the proton hyperfine coupling parameter space is large, and the fitting error function in this high-dimensional space contains a large number of local minima that make direct least-squares fitting approaches fail; therefore, additional restrictions upon the selection of proton couplings is required.

As described in the introduction, the hyperfine coupling parameters for a given proton can be broken apart into the separate contributions from contact coupling and dipolar coupling. Additionally, dipolar coupling can be reasonably well modeled by the point-dipole approximation for most protons in a given vanadyl porphyrin; therefore, the parameter space for hyperfine coupling can be represented as a two-dimensional plane with contact couplings along one axis, and proton–vanadium distances across the other.

Without additional consideration, the two-dimensional parameter space of all possible contact couplings and proton–vanadium distances is massive. Including assumptions about the underlying distribution of hyperfine couplings and reducing the parameter space by pruning accordingly will reduce the size of the parameter space; however, any assumptions being introduced require careful consideration. If the pruning is too conservative, the parameter space will not be significantly reduced in size, but if the pruning is too aggressive, there is a substantial risk of introducing an unidentifiable bias into the analysis.

To determine the maximally accessible region in the parameter space for proton-vanadium distance and contact coupling for vanadyl porphyrins, DFT calculations were made on a subset of known vanadyl porphyrins that account for (as far as this author knows) all structurally distinct types of protons that occur in vanadyl porphyrins within 9 Å of the vanadyl ion. The structures with a subset of protons highlighted are shown in Figure 19. There are hundreds of other vanadyl porphyrins, but they consist of variations upon the structures contained below.

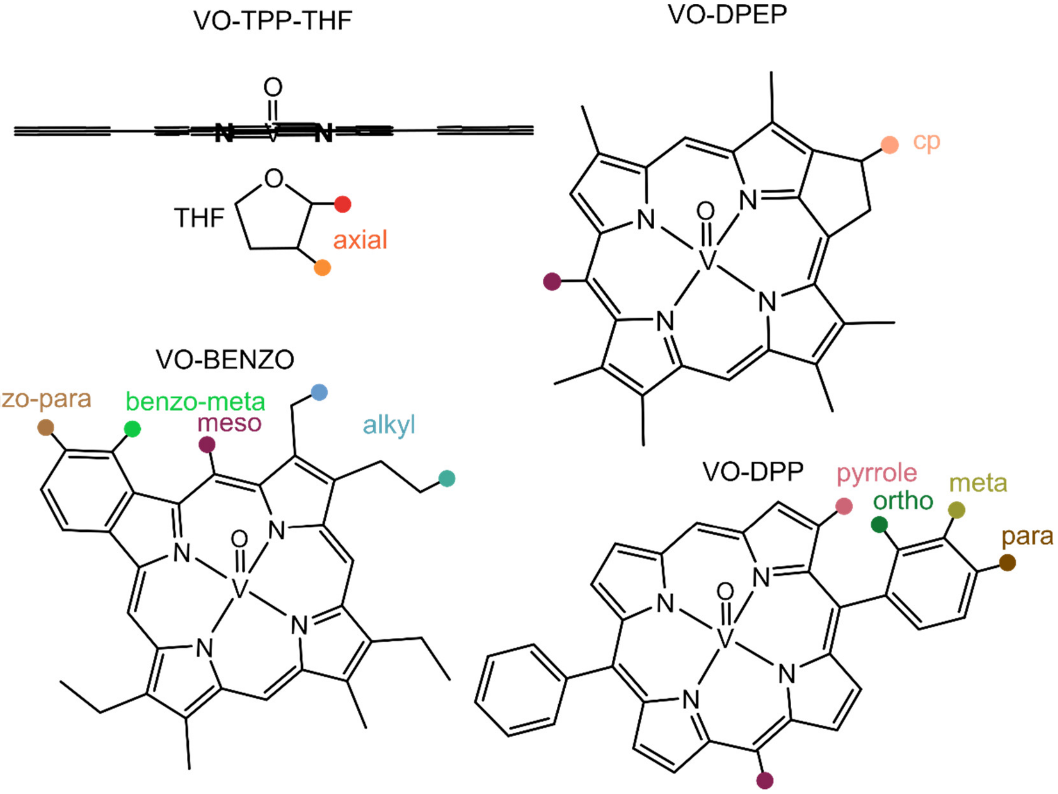

Figure 19. Subset of the structures used to generate the basis set of vanadyl porphyrin proton hyperfine coupling parameters, using DFT. For clarity, only one of each type of proton is highlighted per structure. This subset of structures reflects the entire ensemble of potential proton couplings within 9 Å of the vanadyl ion.

The calculated proton hyperfine couplings are shown below in Figure 20. Most of the parameters follow expected behavior, e.g. negligible contact coupling for protons as their distance from the vanadyl increases. The exception to this trend is the protons attached to THF (bound axially to vanadium from the bottom of the porphyrin plane). Despite being the protons closest to the vanadium, they have a contact coupling similar in magnitude to the most distant protons. This is due to the orientation of the $3d_{xy}$-like orbital of the vanadyl SOMO. The SOMO spreads across, but not significantly above or below the porphyrin plane. The orientation of the orbital further reduces the required parameter space, because the ensemble of molecules that bind to the vanadyl porphyrin base are only significantly coupled through the dipolar interaction, which is purely distance dependent. As seen in Figure 13 DFT calculations match the experimental results of the model compounds relatively well; however to account for any inaccuracies in DFT calculations, and the possibility of previously unknown vanadyl porphyrins, the parameter space for analysis moving forward is spread slightly beyond the calculated parameters. The expansion of the parameter space relative to the calculated parameters is highlighted in Figure 20 with the shaded area.

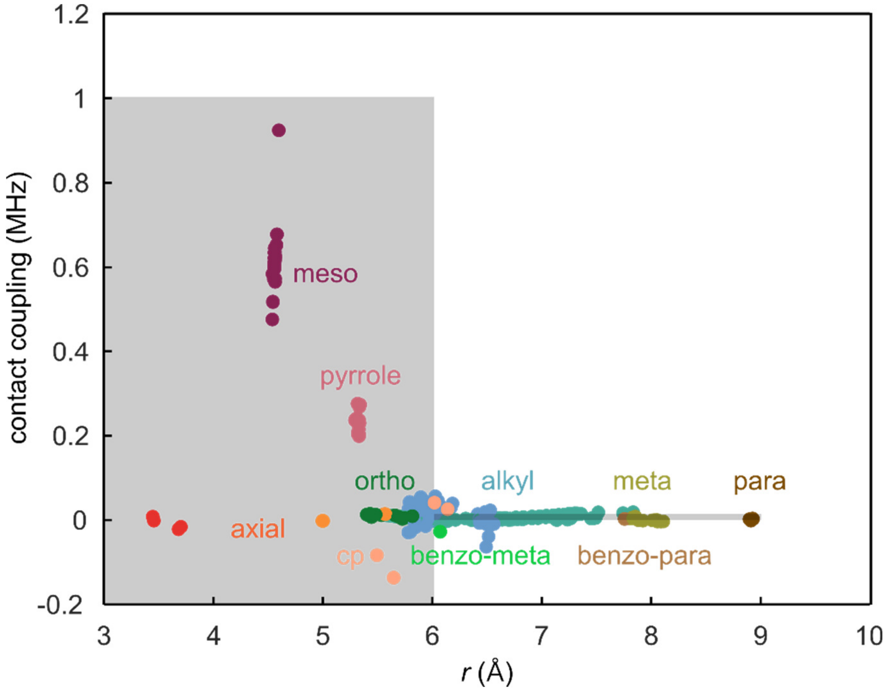

Figure 20. Results of DFT calculation of proton hyperfine coupling parameters. The marker colors match the color selection of the structures shown in above in Figure 19. The shaded area reflects the parameter subspace that is used for basis set construction (see below). The DFT calculations were performed with ORCA 4.1 using the B3LYP functional and EPR-II basis set on all of the atoms except vanadium which utilized the CP(PPP) functional.

The introduction of a pruned parameter space for the hyperfine coupling reduces the complexity of the ENDOR analysis; however, the parameter space is still too large to make meaningful conclusions from the ENDOR spectra. The introduction of further numerical methods to reduce the parameter space is still required. The hyperfine coupling interaction is analogous to the interaction between two unpaired electron spins. A common pulse EPR experiment, double electron-electron resonance (DEER), is one method used to measure the distance between two paramagnetic spin centers coupled to each other via pure dipolar coupling. The DEER experiment yields a trace in the time domain, which is then analyzed to yield an electron–electron distance distribution in the distance domain. The transformation between the time domain and frequency domain is relatively straightforward, but the transformation from the frequency domain to the distance domain fundamentally has the same limitations as transforming ENDOR spectra into the distance domain. There are several approaches to transforming DEER time-domain data into the distance domain. The method that requires the fewest assumptions about the nature of the underlying system uses a non-parametric distance distribution histogram and uses Tikhonov regularization to solve the least-squares fitting problem. This method was initially introduced into magnetic resonance for “de-Pake-ing” NMR spectra,[70] in EPR it is most often used to analyze DEER data.[71] Tikhonov regularization is a form of penalized least-squares fitting, and the mathematical expression is given by

$$P_{\text{fit}} = \underset{P \geq 0}{\operatorname{argmin}}(\|V - KP\|^2 + \alpha^2 \|LP\|^2) \quad (10)$$

where P_{fit} is the fitted distance distribution for a given data set, V is the experimental data, K is the "kernel" which describes how a distance distribution generates the experimental signal; P is the distance distribution; α and L are penalty terms that add additional terms depending on the nature of P. Tikhonov regularization iteratively changes P until the objective function in the above equation is minimized. There exist several approaches to the optimal selection of α and L for the DEER experiment.[72] In this work, we attempt to apply Tikhonov regularization to electron–proton distance distributions via hyperfine coupling through ENDOR.

4.5 TIKHONOV REGULARIZATION OF MODEL VANADYL PORPHYRINS

The attempt to apply Tikhonov regularization in the model vanadyl porphyrins resulted in mixed success. For the alkyl model compounds (VO-EP and VO-OEP) the hyperfine parameters determined through the Tikhonov approach matched the experimental results (not shown); however, as shown in Figure 21, attempting to apply the regularization method to the phenyl porphyrins, the resulting hyperfine couplings deviated significantly from those predicted by the DFT calculations (The DFT values approximate the experimental results, see above).

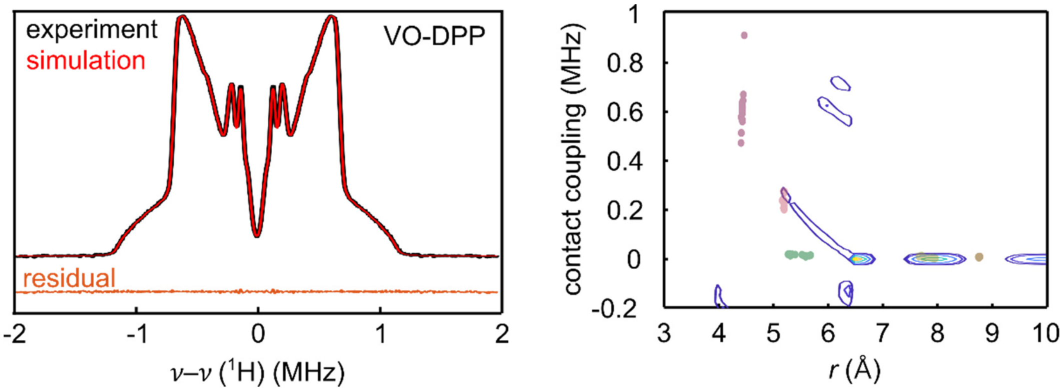

Figure 21. The panel on the left compares the simulation generated by Tikhonov regularization to the experimental spectrum of VO-DPP. The distribution of hyperfine values used to generate the simulation are shown on the right. The deviation from the calculated values (colored circles) demonstrates the remaining over-parametrization of the simulation space.

Despite the failure to produce accurate estimates of hyperfine coupling the regularization approach recreates the experimental spectrum remarkably well. This outcome highlights the remaining over-parametrization of the simulation space even after application of Tikhonov regularization. The failure of the Tikhonov approach to successfully analyze the model spectrum data led to exploration of another approach of least squares penalization.

4.6 BAYESIAN PENALIZED LEAST SQUARES

The utility of Bayesian approaches to data analysis in EPR spectroscopy is becoming more apparent.[73,74] To that end a Bayesian approach towards the analysis of the ENDOR spectra of vanadyl porphyrins in crude oil is being investigated. The advantage that a Bayesian approach provides is in the explicit description of prior knowledge and the effect that prior knowledge has upon analysis of new data.

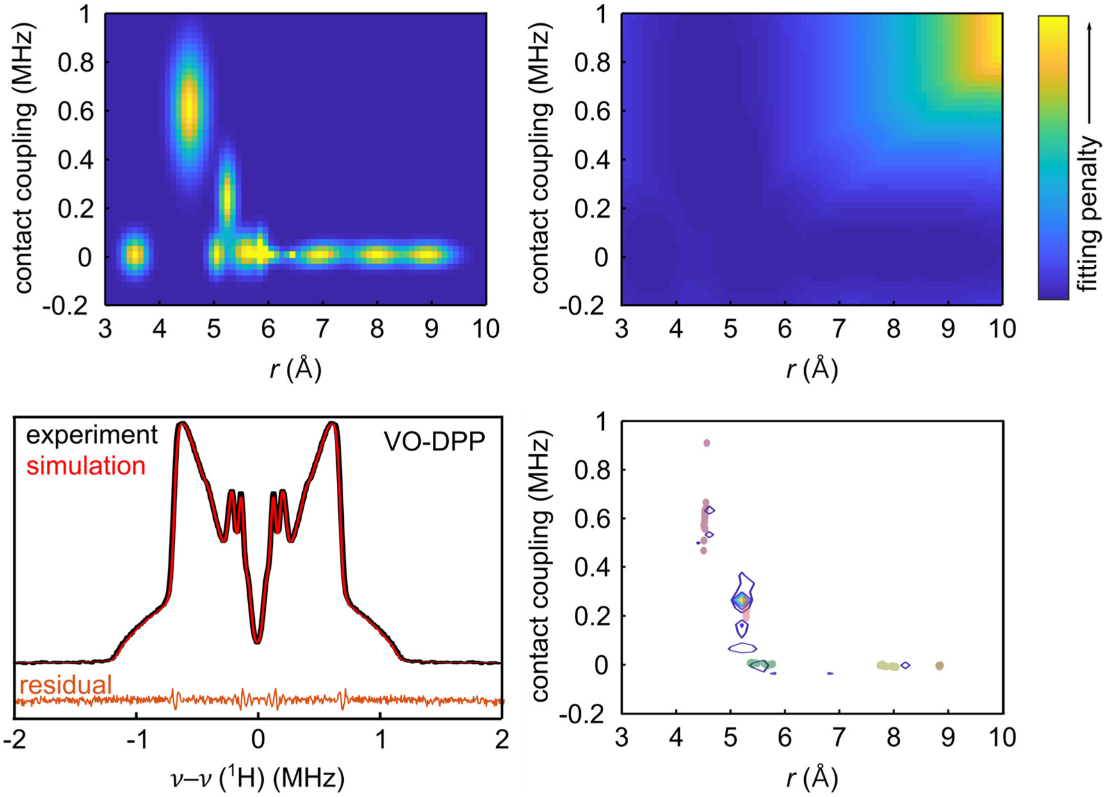

Figure 22. The top left panel is the prior probability distribution of expected proton hyperfine couplings found in vanadyl porphyrins, derived from the DFT values in Figure 20. The top right panel is the two-dimensional penalty function based upon the prior probability distribution. The bottom left panel compares the experimental ENDOR spectrum of VO-DPP with a simulation generated by penalized least-squares fitting. The bottom right panel is a contour plot of the population distribution of hyperfine couplings from the simulation of VO-DPP. The DFT calculations for the groups of protons on VO-DPP are included for comparison with the least-squares fitting values.

To incorporate a Bayesian penalty to the least-squares fitting process, explicit assumptions about the structure of the data are required. The prior knowledge chosen is the distribution of hyperfine coupling in Figure 20, with some allowance for small deviations in particular for the contact coupling. This allowance is applied by Gaussian broadenings along both the contact dimension and the distance dimensions (Figure 22 top left). A penalty function was generated from this prior probability distribution by taking the negative logarithm (Figure 22 top right). As shown in Figure 22 bottom left, applying the Bayesian penalty results in a good fit to the data despite the significant restrictions. Figure 22 bottom right shows that it results in a more parsimonious analysis of the model compounds than the Tikhonov approach displayed above.

These initial results of the Bayesian approach are promising; however, the effectiveness of the method is still under investigation with well understood systems prior to moving to the unknown crude oil samples.

4.7 CONCLUSIONS AND FUTURE OUTLOOK

This work is focused on the development of a separation-free method of vanadyl porphyrin analysis. The utility of ENDOR spectroscopy for measuring individual vanadyl porphyrins is demonstrated in the previous chapter. The measurement and analysis of single porphyrins or even simple mixtures is relatively straightforward if pulse-induced broadenings in the ENDOR spectrum are kept negligible. The increased complexity of vanadyl porphyrins in crude oil increases the difficulty of analysis; however, with the application of penalized least squares fitting it is possible to robustly fit spectra from model compounds. This shows that it is potentially possible to apply this method to disentangle and speciate the vanadyl porphyrins in crude oil samples.

This is an ongoing project, and there are additional approaches that have not yet been explored that could further improve the distinction between crude oil samples. The penalized least-squares methodology has only included the orientation non-selective ENDOR spectra. Expanding the method to include the information contained within the orientationally selective ENDOR spectra should further reduce the parameter space and improve the fitting results.

Penalized least-squares fitting is one of the more popular methods of analyzing data; however, there are other methods that can yield similar but distinct distance distributions.[75] A global approach involving multiple methods could yield information that is not obtainable via one approach alone.

References

(1) Schweiger, A.; Jeschke, G. *Principles of Pulse Electron Paramagnetic Resonance*; 2001.

(2) Feher, G. *Phys. Rev.* **1956**, *103*, 834–835.

(3) Davies, E. R. *Phys. Lett. A* **1974**, *47* (1), 1–2.

(4) Mims, W. B. *Proc. R. Soc. A Math. Phys. Eng. Sci.* **1965**, *283* (1395), 452–457.

(5) Larocca, M.; De Lasa, H. I.; Farag, H. I.; Ng, S. *Ind. Eng. Chem. Res.* **1990**, *29* (11), 2181–2191.

(6) Lauritsen, J. V.; Nyberg, M.; Nørskov, J. K.; Clausen, B. S.; Topsøe, H.; Lægsgaard, E.; Besenbacher, F. *J. Catal.* **2004**, *224* (1), 94–106.

(7) Mills, G. A. *Ind. Eng. Chem.* **1950**, *42* (1), 182–187.

(8) Waluk, J. *Chem. Rev.* **2016**, acs.chemrev.6b00328.

(9) Ali, M. F.; Abbas, S. *Fuel Process. Technol.* **2006**, *87* (7), 573–584.

(10) Gourier, D.; Delpoux, O.; Bonduelle, A.; Binet, L.; Ciofini, I.; Vezin, H. *J. Phys. Chem. B* **2010**, *114* (10), 3714–3725.

(11) Dunning, H. N.; Rabon, N. A. *Ind. Eng. Chem.* **1956**, *48* (5), 951–955.

(12) Kim, C. S.; Massoth, F. E. *Fuel Process. Technol.* **1993**, *35* (3), 289–302.

(13) Mckenna, A. M.; Williams, T.; Putman, J. C.; Aeppli, C.; Reddy, C. M.; Valentine, D. L.; Lemkau, K. L.; Kellermann, M. Y.; Savory, J. J.; Kaiser, N. K.; Marshall, A. G.; Rodgers, R. P. *Energy & Fuels* **2014**, *28*, 2454–2464.

(14) Mamin, G. V.; Gafurov, M. R.; Yusupov, R. V.; Gracheva, I. N.; Ganeeva, Y. M.; Yusupova, T. N.; Orlinskii, S. B. *Energy & Fuels* **2016**, *30* (9), 6942–6946.

(15) Ben Tayeb, K.; Delpoux, O.; Barbier, J.; Marques, J.; Verstraete, J.; Vezin, H. *Energy & Fuels* **2015**, *29* (7), 4608–4615.

(16) Dechaine, G. P.; Gray, M. R. *Energy & Fuels* **2010**, *24* (5), 2795–2808.

(17) Zhao, X.; Xu, C.; Shi, Q. *Porphyrins in Heavy Petroleums: A Review. In: Structure and Modeling of Complex Petroleum Mixtures. Structure and Bonding, vol 168.*; Xu, C., Shi, Q., Eds.; Springer, Cham, 2015.

(18) Dunning, H. N.; Moore, J. W.; Bieber, H.; Williams, R. B. *J. Chem. Eng. Data* **1960**, *5* (4), 546–549.

(19) Gilinskaya, L. G. *J. Struct. Chem.* **2008**, *49* (2), 245–254.

(20) Premovic, P. I.; Allard, T.; Nikolic, N. D.; Tonsa, I. R.; Pavlovic, M. S. *Fuel* **2000**, *79* (7), 813–819.

(21) Premović, P. I.; Dordević, D. M.; Pavlović, M. S. *Fuel* **2002**, *81* (15), 2009–2016.

(22) Gerfen, G. J.; Hanna, P. M.; Chasteen, N. D.; Singel, D. J. *J. Am. Chem. Soc.* **1991**, *113* (25), 9513–9519.

(23) Saraceno, A. J.; Fanale, D. T.; Coggeshall, N. D. *Anal. Chem.* **1961**, *33* (4), 500–505.

(24) Galtsev, V. E.; Ametov, I. M.; Grinberg, O. Y. *Fuel* **1995**, *74* (5), 670–673.

(25) Biktagirov, T.; Gafurov, M.; Mamin, G.; Gracheva, I.; Galukhin, A.; Orlinskii, S. *Energy and Fuels* **2017**, *31* (2), 1243–1249.

(26) Barwise, A. J. G. *Energy & Fuels* **1990**, *4* (1), 647–652.

(27) Mitchell, D. L.; Speight, J. G. *Fuel* **1973**, *52* (2), 149–152.

(28) Treibs, A. *Angew. Chem.* **1936**, *49* (38), 682–686.

(29) Lash, T. D. *Macroheterocycles* **2008**, *1* (1), 9–20.

(30) Fish, R. H.; Komlenic, J. J. *Anal. Chem.* **1984**, *56* (3), 510–517.

(31) Premović, P. I.; Pavlović, M. S.; Pavlović, N. Z. *Geochim. Cosmochim. Acta* **1986**, *50* (9), 1923–1931.

(32) *The Role of Trace Metals in Petroleum*; Yen, T. F., Ed.; Ann Arbor Science: Ann Arbor MI, 1975.

(33) Abdula, R. A.; Hakimi, M. H.; Ismail, L. A.; Mina, C. T. **2018**, *14* (2), 71–80.

(34) Qian, K.; Mennito, A. S.; Edwards, K. E.; Ferrughelli, D. T. *Rapid Commun. Mass Spectrom.* **2008**, No. 22, 2153–2160.

(35) Ballhausen, C. J.; Gray, H. B. *Inorg. Chem.* **1962**, *1* (1), 111–122.

(36) Grant, C. V.; Geiser-Bush, K. M.; Cornman, C. R.; Britt, R. D. *Inorg. Chem.* **1999**, *38* (26), 6285–6288.

(37) Kivelson, D.; Sai-Kwing, L. *J. Chem. Phys.* **1964**, *41* (7), 1896–1903.

(38) Dickson, F. E.; Kunesh, C. J.; Mcginnis, E. L.; Petrakis, L. *Anal. Chem.* **1972**, *44* (6), 978–981.

(39) Buckmaster, A.; Malhotra, M. *Fuel* **1985**, *64*, 335–341.

(40) Gascon, G.; Negrin, J.; Garcia-Montoto, V.; Acevedo, S.; Lienemann, C. P.; Bouyssiere, B. *Energy and Fuels* **2019**, *33* (3), 1922–1927.

(41) Fish, R. H.; Komlenic, J. J.; Wines, B. K. *Anal. Chem.* **1984**, *56* (13), 2452–2460.

(42) Rytting, B. M. K.; Singh, I. D.; Kilpatrick, P. K.; Harper, M. R.; Mennito, A. S.; Zhang, Y. *Energy and Fuels* **2018**, *32* (5), 5711–5724.

(43) Qian, K.; Fredriksen, T. R.; Mennito, A. S.; Zhang, Y.; Harper, M. R.; Merchant, S.; Kushnerick, J. D.; Rytting, B. M. K.; Kilpatrick, P. K. *Fuel* **2019**, *239*, 1258–1264.

(44) McKenna, A. M.; Williams, J. T.; Putman, J. C.; Aeppli, C.; Reddy, C. M.; Valentine,

D. L.; Lemkau, K. L.; Kellermann, M. Y.; Savory, J. J.; Kaiser, N. K.; Marshall, A. G.; Rodgers, R. P. *Energy & Fuels* **2014**, *28* (4), 2454–2464.

(45) Biktagirov, T. B.; Gafurov, M. R.; Volodin, M. A.; Mamin, G. V; Rodionov, A. A.; Izotov, V. V; Vakhin, A. V; Isakov, D. R.; Orlinskii, S. B. **2014**.

(46) Gafurov, M. R.; Volodin, M. A.; Rodionov, A. A.; Sorokina, A. T.; Dolomatov, M. Y.; Petrov, A. V.; Vakhin, A. V.; Mamin, G. V.; Orlinskii, S. B. *J. Pet. Sci. Eng.* **2018**, *166*, 363–368.

(47) Benamsili, L.; Korb, J. P.; Hamon, G.; Louis-Joseph, A.; Bouyssiere, B.; Zhou, H.; Bryant, R. G. *Energy & Fuels* **2014**, *28* (3), 1629–1640.

(48) Biktagirov, T.; Gafurov, M. R.; Mamin, G. V.; Gracheva, I. N.; Galukhin, A. V.; Orlinskii, S. B. *Energy & Fuels* **2017**, *31* (2), 1243–1249.

(49) Gracheva, I. N.; Gafurov, M. R.; Mamin, G. V; Biktagirov, T.; Rodionov, A. A.; Galukhin, A. V.; Orlinskii, S. B. *Magn. Reson. Solids* **2016**, *18* (1), 1–5.

(50) O'Reilly, D. E. *J. Chem. Phys.* **1959**, *30* (2), 591.

(51) Mannikko, D.; Stoll, S. *Energy and Fuels* **2019**, *33* (5), 4237–4243.

(52) McKenna, A. M.; Purcell, J. M.; Rodgers, R. P.; Marshall, A. G. *Energy & Fuels* **2009**, *23* (4), 2122–2128.

(53) Stoll, S.; Schweiger, A. *J. Magn. Reson.* **2006**, *178* (1), 42–55.

(54) Hoffman, B. M.; DeRose, V. J.; Ong, J. L.; Davoust, C. E. *Journal of Magnetic Resonance, Series A*. 1994, pp 52–57.

(55) Molinaro, F.; Ibers, J. *Inorg. Chem.* **1976**, *15* (9), 2278–2283.

(56) Drew, M. G. B.; Mitchell, P. C. H.; Scott, C. E. *Inorg. Chim. Acta* **1984**, *82* (1), 63–68.

(57) Neese, F. *Wiley Interdiscip. Rev. Comput. Mol. Sci.* **2012**, *2* (1), 73–78.

(58) Becke, A. D. *Phys. Rev. A* **1988**, *38* (6), 3098–3100.

(59) Grimme, S.; Antony, J.; Ehrlich, S.; Krieg, H. *J. Chem. Phys.* **2010**, *132* (15).

(60) Grimme, S.; Ehrlich, S.; Goerigk, L. *J. Comput. Chem.* **2011**, *32*, 1456–1465.

(61) Schäfer, A.; Horn, H.; Ahlrichs, R. *J. Chem. Phys.* **1992**, *97* (4), 2571–2577.

(62) Schäfer, A.; Huber, C.; Ahlrichs, R. *J. Chem. Phys.* **1994**, *100* (8), 5829.

(63) Becke, A. D. *J. Chem. Phys.* **1993**, *98* (2), 1372.

(64) Becke, A. D. *J. Chem. Phys.* **1993**, *98* (7), 5648.

(65) Lee, C.; Yang, W.; Parr, R. G. *Phys. Rev. B* **1988**, *37* (2), 785–789.

(66) Stephens, P. J.; Devlin, F. J.; Chabalowski, C. F.; Frisch, M. J. *J. Phys. Chem.* **1994**, *98* (45), 11623–11627.

(67) Rega, N.; Cossi, M.; Barone, V. *J. Chem. Phys.* **1996**, *105* (24), 11060–11067.

(68) Neese, F. *Inorg. Chim. Acta* **2002**, *337* (1), 181–192.

(69) Goldfarb, D.; Epel, B.; Poppl, A.; Manikandan, P.; Vega, S. *J. Magn. Reson.* **2001**, *148* (2), 388–397.

(70) Schäfer, H.; Mädler, B.; Volke, F. *J. Magn. Reson. Ser. A* **1995**, *116* (2), 145–149.

(71) Jeschke, G.; Chechik, V.; Ionita, P.; Godt, A.; Zimmermann, H.; Banham, J.; Timmel, C. R.; Hilger, D.; Jung, H. *Appl. Magn. Reson* **2006**, 30, 473–498.

(72) Edwards, T. H.; Stoll, S. *J. Magn. Reson.* **2018**, *288*, 58–68.

(73) Sweger, S. R.; Pribitzer, S.; Stoll, S. *J. Phys. Chem. A* **2020**, *124* (30), 6193–6202.

(74) Edwards, T. H.; Stoll, S. *J. Magn. Reson.* **2016**, *270*, 87–97.

(75) Hustedt, E. J.; Marinelli, F.; Stein, R. A.; Faraldo-Gomez, J. D.; Mchaourab, H. S. *Biophys. J.* **2018**, *115*, 1200–1216.